THE JOURNAL OF PHYSICAL CHEMISTRY B

Article

pubs.acs.org/JPCB

Pressure-Dependent Properties of Elementary Hydrophobic Interactions: Ramifications for Activation Properties of Protein Folding

Cristiano L. Dias*[,§,‡] and Hue Sun Chan*[,‡]

[§]Department of Physics, New Jersey Institute of Technology, University Heights, Tiernan Hall, Room 463, Newark, New Jersey 07102, United States

[‡]Departments of Biochemistry, Molecular Genetics, and Physics, University of Toronto, 1 King's College Circle, Toronto, Ontario Canada M5S 1A8

Supporting Information

ABSTRACT: Hydration effects on a pair of methane molecules are investigated by extensive constant-pressure (NPT) sampling using the TIP4P model of water under 1, 1000, 2000, and 3000 atm. The volume distributions of pure water and of methanes plus water are determined directly as functions of methane−methane distance ξ. The corresponding excess isothermal and adiabatic compressibilities are estimated from the pressure-dependent methane excess volume. The dependence of excess volume on ξ is oscillatory for small ξ. The maxima of excess volume and compressibility are seen near the desolvation barrier (db) of the potential of mean force (PMF). These features may be understood by the development, near the db, of a void volume encased by a molecular (Connolly) surface defined using a water-sized probe. These db properties for two methanes are consistent with well-corroborated experimental observations of positive activation volumes for protein folding and some experiments suggesting a slightly higher compressibility for the folding transition state than the unfolded state. At high pressures, the volumes at the PMF solvent-separated minimum and the contact-minimum configurations are both smaller than the volume at large ξ. This trend provides a rationalization for the compactness of pressure-denatured states of proteins. Taking the packing densities of pure nonpolar phases into consideration, our simulation results suggest that whether the activation volume of unfolding is positive or negative hinges on the packing compactness of the protein core. Volume change can be but is not necessarily monotonic along the folding pathway.

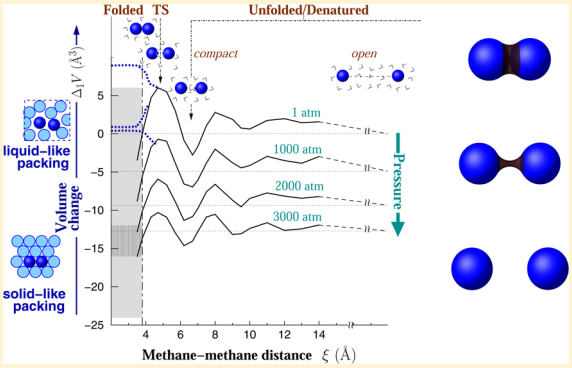

I. INTRODUCTION

With its unique physicochemical properties, water mediates biomolecular interactions,[1,2] and thus is crucial for life on Earth.[3] In particular, the effective attraction between nonpolar molecules in aqueous environments is a major driving force in protein folding and other self-assembly events in biology.[4−11] For this reason, various aspects of hydrophobic interactions have been widely studied;[12−16] however, much remains to be elucidated.

Hydrophobic interactions are modulated by aqueous solvent conditions such as temperature, pressure, and cosolvents. An intuitive, semiquantitative physical approach to probe the role of hydrophobic interactions in biomolecular processes has been to relate configurational transitions in biomolecules induced by various changes in solvent conditions to corresponding variations in hydrophobic effects of small, "model-compound" molecules.[17−22] Such an approach was used to study the effects of temperature,[23−27] salt,[28,29] denaturants,[30−33] and osmolytes.[34] Pressure dependence has been tackled in a similar vein, leading to notable advances.[35−43] Compared to temperature and denaturant, however, less attention has been paid to pressure dependence of elementary hydrophobic interactions and its ramifications on volumetric aspects of protein folding. In particular, few computational studies have utilized direct simulation of volume changes associated with pertinent hydration processes.[42,44−49] The present work builds on a study that directly simulated the volumes of a single methane in water under pressures ranging from 1 to 3000 atm.[42] Here we develop a similar computational methodology for a two-methane pair.[50] Our main goal is to use the new findings to gain insight into experimental data on pressure-induced protein conformational transitions.[21,51−88]

Simulation of a pair of nonpolar solutes is valuable because it provides a wealth of two-body information that cannot be derived from experimental data on bulk hydrophobic effects or simulation of a single nonpolar solute.[89] Indeed, recent atomic

Received: February 24, 2014
Revised: June 15, 2014
Published: June 16, 2014

   dx.doi.org/10.1021/jp501935f | J. Phys. Chem. B 2014, 118, 7488−7509

simulations of pairwise hydrophobic interactions have provided rationalizations for several intriguing phenomena in protein folding, including residual intraprotein contacts at high urea concentrations,[31,90,91] that would have been puzzling from a perspective based solely upon bulk hydrophobicity. Another case in point is the desolvation barriers that contribute to the rate-limiting step,[92,93] cooperativity,[94−96] the tremendous diversity in experimental folding rates,[97−101] and secondary structure preference[102,103] in protein folding. Desolvation barrier is a robust feature in the two-body hydrophobic potential of mean force (PMF),[50] but by definition, it is not a property of single-solute hydration.

Recent atomic simulations indicate further that comparisons of pairwise hydrophobic interactions between solutes of difference sizes can yield critical insights into folding energetics. In this regard, water-mediated interactions between large nonpolar solutes exhibit properties more akin—though not identical—to bulk hydrophobicity than small-molecule-pair hydrophobic interactions.[89] For instance, at room temperature, folding transition states of small proteins typically have a lower heat capacity but a significantly higher enthalpy than that of the unfolded state.[104] Whereas the enthalpic barrier to folding does not follow from the prevalent understanding of bulk hydrophobicity, the lower heat capacity of the folding transition state relative to that of the unfolded state is consistent with a simple physical picture based upon bulk hydrophobicity and the expected lower hydrophobic exposure in the transition state than in the unfolded state. Interestingly, the experimental trends of enthalpy and heat capacity variation along the folding pathway are both captured by the association of two relatively large hydrophobic solutes in the form of polyleucine α-helices.[105] The enthalpy trend is also observed, albeit to a lesser extent, in the association of two β-strands with large hydrophobic side chains.[103] Indeed, recent simulations suggest that a prominent enthalpic barrier similar to that observed in protein folding is likely a general, robust feature in the association of large nonpolar solutes: Such a feature has been observed not only for two α-helices simulated using the TIP4P water model and the OPLS force field[105] but also for two graphite-like plates simulated using the SPC/E water model and the AMBER force field.[106] In contrast, the heat capacity and enthalpy trends of protein folding are not captured by the association of two small nonpolar solutes. The latter exhibits only a small enthalpic barrier[27,95] and a distance-dependent heat capacity profile that attains its highest value near the desolvation barrier position[24−27]—rather than adopting at this position an intermediate heat capacity value between the large- and small-distance values, as one might expect from drawing a naïve connection to protein folding.

Despite its difference with the trend seen along folding pathways, this hitherto unexpected behavior of simulated heat capacity for two small nonpolar solutes provides a novel rationalization[31] for a peculiar heat capacity "retardation" phenomenon observed in folding experiments.[107] Taken together, the contrast between simulated small- and large-solute properties bears on the general question of length-scale dependence of hydrophobic interactions[106,108−111] and is highly suggestive of a local−nonlocal cooperative folding mechanism.[100,112,113] Of particular relevance to our present effort is that the activation volumes for the association of two hydrophobic α-helices[105] or two hydrophobic β-strands[103] are of the same order of magnitude[99] as experimentally determined activation volumes of folding.[82] This finding suggests that the void volume created when two or more large parts of a protein chain approach one another cooperatively during folding is a major physical origin of the experimentally observed folding activation volume.[100] Here we will compare various volumetric signatures for the association of a pair of small nonpolar solutes in water with the corresponding signatures for protein folding.

Pressure effects on proteins are directly relevant to biology of the deep ocean and subseafloor sedimentary microbes[114] as well as to the study of possible conditions under which early life might have evolved on Earth.[115] More generally, pressure, like temperature, is a basic intensive physical property that can be used to probe biomolecular properties. Pressure and volume are conjugate thermodynamic variables. In accordance with Le Chatelier's principle, increasing pressure shifts the equilibrium of a system toward configurations with smaller volumes. It has been known for a century that pressure can denature proteins.[51] Indeed, this fact had contributed to the first recognition in the early 1930s that protein denaturation corresponds to unfolding of a chain molecule.[116,117] Since the 1950s, pressure and volumetric effects on protein conformations have been studied continuously.[52,53,56,57] Although interpretation of experiment is at times controversial, a repertoire of information has been amassed. One general trend is that the volume change of proteins upon unfolding is small ($\lesssim$ 2% of the partial molar volume of the folded structure)[55,118] and that the volume change is mostly negative.[55,60] However, the volume change can be positive[60] at low pressures, but it is invariably negative at high pressures.[74] Another typical observation is that pressure-denatured states have residual structures[58,62] and are generally more compact than heat-denatured states.[85]

It has long been known, however, that the pressure-dependent volume change upon protein unfolding is at odds with the volume changes that accompany transfers of nonpolar model compounds from organic solvents to water:[4,119] Although the exact transfer volume depends on the model compound and the solvent,[4,120,121] volume changes for transfers from organic solvent to water are consistently large and negative at low pressures[120−122] but positive at high pressures.[122] Hydration of hydrogen bonds[123] and peptide groups[84] are also seen to have negative volume contributions to unfolding. Therefore, unlike the success in rationalizing heat denaturation of proteins by model compound transfer data, there is an obvious mismatch between the mostly small negative volume changes observed in protein unfolding and the large negative volume changes for transfers of hydrophobic compounds from organic solvents to water.[4,119] This discrepancy, referred to as the "protein volume paradox",[118] has largely been resolved by realizing that inasmuch as volumetric effects are concerned, organic solvents are not a good model for the folded protein core.[124] This is clear from the fact that folded proteins are less compressible than water, but organic solvents are much more compressible than water.[14,122] It follows that a physical account of pressure effects on folding must consider the void volume in the folded protein, its compressibility, and the difference in "thermal volume"[118] between the folded and unfolded states.[84,87]

In contrast to the difficulty in using bulk hydrophobicity to rationalize pressure-dependent protein folding behaviors, knowledge of pair hydrophobic interaction properties have helped make important advances in understanding the pressure-denatured state. In an insightful simulation study of two- and three-methane PMFs by the SPC water model in 1998, the PMF solvent-separated minimum was found to

deepen with pressure and become less unfavorable relative to the contact minimum.[38] This result led the authors to conclude that "pressure denaturation corresponds to the incorporation of water into the protein, whereas heat denaturation corresponds to the transfer of nonpolar groups into water".[38] In this picture, water penetration of the protein core[125] increases with pressure,[38,58,126] as envisioned 80 years ago in the seminal work on protein denaturation by Wu, who wrote that "when a protein solution is subjected to high pressure, molecules of water are crushed into the protein molecule and cause denaturation".[116] Accordingly, the pressure-denatured state is expected to be compact, with nonpolar residues solvated by a thin layer of water. This perspective rationalizes experimental findings that pressure-denatured states contain native and/or nonnative secondary structures and, like cold-denatured states,[127] are compact albeit swollen compared to the native state.[58,62,68,85,128−130] The idea has since been utilized in numerous theoretical investigations, including a procedure for constructing a pressure-denatured state for molecular dynamics simulation,[45] simulation of low-temperature- and high-pressure-induced swelling of a hydrophobic homopolymer[131] and computational studies of the relationship between pressure[132] and cold denaturation[132−135] using a two-dimensional water model.[136] Conceptually, however, it is important to recognize that two- and three-methane PMFs do not, by themselves, necessarily provide an adequate physical picture of pressure denaturation because the two- and three-body contact minima retain significant water exposure. Hence, the adequacy of these configurations as models for the sequestered folded protein core can be limited. Nonetheless, the pressure dependence of two- and three-body PMFs do capture important physical trends that have been verified by simulation of homopolymers configured in two[132] and three[131] dimensions.

An important aspect of volumetric properties of protein folding that has not been addressed much by model compound investigations or atomic simulation is the pressure dependence of folding/unfolding kinetics. Pressure-dependent unfolding kinetics was quantified by turbidity measurements as early as 1960 in a study of ovalbumin and carbonylhemoglobin.[53] Studies on different proteins since then have shown that the activation volume for folding is almost always positive.[61,65,66,69,72,73,78−80] The activation volume for unfolding, however, is often negative,[65,69,72,78−80] though under some conditions it can be positive for some proteins.[61,72] Unlike the clear pattern in the temperature/denaturant dependence of the folding kinetics of single-domain proteins[137,138] which is amenable to a general rationalization in terms of desolvation effects,[95,139−141] the temperature/pressure dependence of folding kinetics is complex. As a result, a general physical perspective is lacking and much remains to be deciphered. In this context, a main goal of the present study is to gain insight into the physical origin of the folding/unfolding activation volume by comparing and contrasting two-methane PMF properties with experimental pressure-dependent folding kinetics data.

In the same vein, we also aim to address the compressibility signature of the folding/unfolding transition state. Comparison of compressibility measurements of model compounds[76,142] and of the proteins can be used to probe conformational changes because the partial molar compressibility of a protein depends on intrachain packing and the hydration environment.[64,68,71,76,143] The core of a folded protein is well-packed and possibly solid-like.[144] Under ambient conditions, compressibilities of folded proteins [$\sim 3-25 \times 10^{-6}$ atm^{-1} (refs 67,70,145,146)] are significantly smaller than that of water [45×10^{-6} atm^{-1} (ref 147)] or most organic liquids [$22-130 \times 10^{-6}$ atm^{-1} (ref 145)]. Rather, they are comparable with the compressibilities of hard polymers ($12-20 \times 10^{-6}$ atm^{-1})[145] and the less compressible species among solid organic materials including molecular crystals [$6.5-40 \times 10^{-6}$ atm^{-1} (ref 145); $\sim 30 \times 10^{-6}$ atm^{-1} for crystalline hydrocarbon[148]]. On the basis of a survey of thermodynamic data, it has been proposed that different types of conformational transitions are characterized by typical signs and magnitudes of compressibility changes.[76,149] Although less data are available for folding kinetics than for thermodynamics, a few experimental observations of a marked decrease in activation volume of unfolding with pressure[53] and a slightly nonlinear dependence of logarithmic folding rate on pressure[80] suggest that the folding/unfolding transition state may be more compressible than either of the folded and unfolded states. Building on a previous study of compressibility of single-methane hydration by our group,[42] here we extend our effort also onto distance-dependent compressibility of two-methane association and its implications on the volumetric properties of the folding transition state.

II. MODELS AND METHODS

All atomic simulation results presented in this work were obtained by NPT Monte Carlo sampling of a system consisting of zero, one, or two methanes embedded among $N = 746$ TIP4P water molecules in a box with variable box size and periodic boundary conditions (Figure 1). As in previous studies by our group,[24,25,27,42] methane molecules were modeled by the united-atom description of Jorgensen et al.,[150] and the software BOSS version 4.1[151] was used for sampling with a cutoff distance for Lennard-Jones interactions set to 10.0 Å.

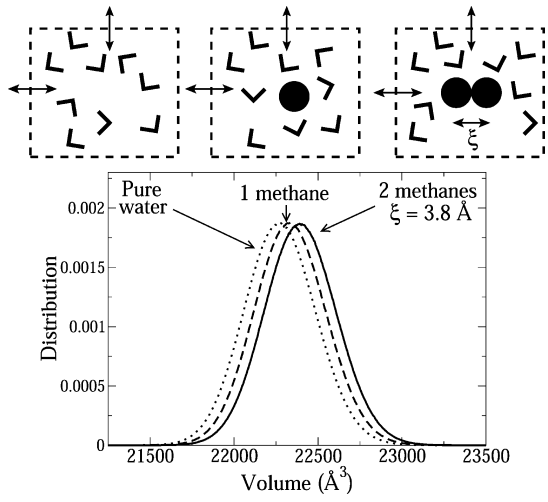

Figure 1. Volume variations of methane plus water systems determined by NPT simulations. Top: schematics of (from left to right) pure water, one methane plus water, and two methanes plus water systems investigated in this study. Water and methane molecules are depicted, respectively, as V-shapes and filled circles. The arrows indicate volume fluctuations during the simulations. Bottom: distributions of volume of simulation boxes containing no methane (pure water; dotted curve), one methane (dashed curve), and two methanes that are at a distance $\xi = 3.8$ Å from each other (solid curve). Data shown are for $T = 298.15$ K, $P = 1$ atm.

dx.doi.org/10.1021/jp501935f | J. Phys. Chem. B 2014, 118, 7488−7509

Simulations were performed at absolute temperatures T = 278.15, 298.15, and 318.15 K (5°, 25°, and 45 °C) and at four different pressures P = 1, 1000, 2000, and 3000 atm. Modeling and methodological details are provided in the online Supporting Information (SI).

III. RESULTS

A. Volume of Single Methane in Water. Using the formulation in SI, the simulated average volume of pure water $\langle V\rangle_N$ and average volume $\langle V\rangle_{N,a}$ of water plus a single methane at a fixed position are shown in Figure 2 for four different pressures. The difference between these two quantities yields the pressure-dependent excess volume (ΔV) data points in the inset (the vertical scale in the inset is different from that in the main plot). Each set of P-dependent data points in Figure 2 was fitted to the quadratic equation eq S9 in SI. The fitted curves were used to determine the partial molar volume V_m (dashed curve in inset) by applying eqs S10 and S11 in SI.

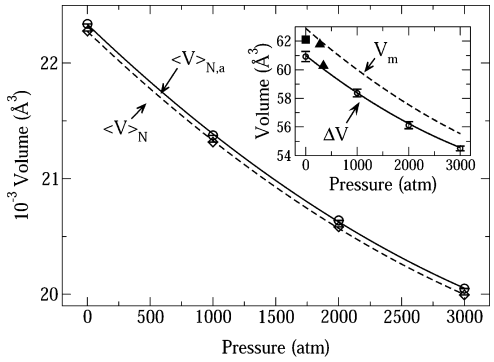

Figure 2. Pressure dependence of excess and partial molar volume of methane in water at T = 298.15 K. Average volume is shown for N = 746 water molecules ($\langle V\rangle_N$ for pure water; diamonds) and the same number of water molecules plus one single methane at a fixed position ($\langle V\rangle_{N,a}$; circles). The dashed and solid curves are best quadratic fits [eq S9 in SI] to the respective data points. Error bars were computed using block averages[160] (see SI). Inset: simulated data points for excess volume $\Delta V = \langle V\rangle_{N,a} - \langle V\rangle_N$ (circles) are fitted to eq S9 (solid curve). The corresponding partial molar volume V_m [eq S7] is also shown (eq S11, dashed curve). Experimental data from Masterton[120] at 1 atm (square) and from Hnědkovský et al.[158] at 276.3 and 345.4 atm (triangles) are included for comparison.

It is instructive to compare the present simulated value of isothermal compressibility κ_T^0 for pure water (eq S10) and V_m of a single methane (eq S11) with experimental and simulation results in the literature. At P = 1 atm and T = 298.15 K, our simulated $\kappa_T^0 = 4.66 \times 10^{-5}$ atm^{-1} is within approximately 1.5% from the experimental value of 4.5888×10^{-5} atm^{-1} reported by Kell.[147] In this regard, our simulated κ_T^0 is closer to the experimental isothermal compressibility and is lower than previously reported TIP4P-simulated κ_T^0 values (in units of 10^{-5} atm^{-1}) of 5.00 (ref 36), 5.98 (ref 152) 5.13, 4.78 (ref 42), and 5.35 (ref 153). Most of the reported simulated κ_T^0 values obtained using other water models are in a similar range (again in units of 10^{-5} atm^{-1}): 6.0 (ref 154) for SPC; 6.4 (ref 154) for TIP3P; 4.20 (ref 155) and 4.67 (ref 153) for SPC/E; 4.81 (ref 156) and 4.87 (ref 152) for TIP4P/Ew; 4.71 (ref 152) and 4.69 (ref 153) for TIP4P/2005; and 4.10 (ref 152) and 5.78 (ref 153) for TIP5P.

The partial molar volume of a single methane obtain using eq S7 and our simulated κ_T^0 at P = 1 atm and T = 298.15 K is 62.79 Å^3. This value is within approximately 1.5% from the experimental V_m of 61.9 Å^3 reported by Masterton.[120] Our simulated V_m is in agreement with previously simulated values of 59.7−63.10 Å^3 obtained by our group.[42] The corresponding NPT-simulated excess volume ΔV at 1 atm obtained here is 60.92 ± 0.35 Å^3, which is also consistent with the 58.3 ± 6.5 Å^3 value computed previously using an NVT ensemble of TIP4P water at ρ^0 = 1 g cm^{-3} (ref 36). For protein-related applications, it is useful to note that the partial molar volume at 298.15 K and 1 atm of an alanine side chain estimated from the V_m difference between alanine and glycine[157] is approximately 28 Å^3 which is about one-half of the V_m of a methane molecule.

The pressure dependence of methane V_m is shown in the inset of Figure 2. The present simulation data show a monotonic decrease of V_m with increasing P. This trend is consistent with the experimental data for 28 and 35 MPa (276.3 and 345.4 atm) reported by Hnědkovský et al.,[158] although the two experimental V_m values exhibit a steeper decrease with only a modest ∼70 atm increase in P than the more gradual trend predicted by simulation. A similar trend of decreasing simulated V_m of methane with increasing P has also been obtained using the TIP3P model at T = 305 K as well as T = 478 K.[159] In contrast, a previous study by our group suggested a small increase in V_m from P = 1 atm to P = 1000 atm. However, that conclusion was noted as only tentative because sampling uncertainties were large at approximately ±3.7 Å^3 (ref 42). With much more extensive sampling, the current numerical uncertainties as estimated by block averages[160] in Figure 2 are much smaller. Thus, the present simulation data provide conclusive support that methane V_m is monotonically decreasing from P = 1 to 3000 atm in our TIP4P model.

B. Compressibility of Single Methane in Water. We next consider the effect of methane on the compressibility of various water plus methane systems (Figure 3). As described in SI, isothermal compressibility were independently computed by

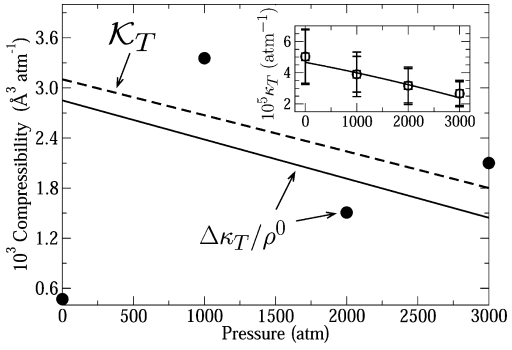

Figure 3. Pressure dependence of simulated partial molar and excess isothermal compressibilities of methane in water at T = 298.15 K. Partial molar isothermal compressibility ($\mathcal{K}_T$, eq S17) was computed using the volume-fitting method in eqs S15, S18, and S20 (dashed curve). The excess isothermal compressibility $\Delta\kappa_T$ in the quantity $\Delta\kappa_T/\rho^0$ was computed from fitted volumes using eq S20 (solid curve) and also from volume fluctuations using eq S19 (filled circles). Inset: pressure dependence of isothermal compressibilities computed from volume fluctuations (eqs S12 and S13) for pure water (κ_T^0, circles) and for methane in water (κ_T^{N+a}, squares) at the same temperature. The corresponding isothermal compressibilities computed from fitted volumes (eqs S10 and S14) are shown by the solid lines. Note that the two fits are too close to be distinguishable in the scale of the present plot. Error bars in the inset are defined in SI.

dx.doi.org/10.1021/jp501935f | J. Phys. Chem. B 2014, 118, 7488−7509

volume fluctuation at a given pressure and also by volume fitting over multiple pressures. The inset in Figure 3 indicates that volume fluctuation and volume fitting give equivalent results for isothermal compressibility within sampling uncertainties. This plot shows that the difference between κ_T^0 for pure water (circles) and κ_T^{N+a} for an aqueous solution with a single methane (square) is small (precise definitions of κ_T^0 and κ_T^{N+a} are provided in SI). This observation is not surprising because a methane solution with mole fraction of $1/(N + 1) = 1/747$ is quite dilute (our simulation box contains 746 water molecules). Both compressibilities show a decreasing trend with increasing P, which is expected because intuitively it should be harder to compress a volume further when it has already been compressed by high pressure.

Changes in the isothermal compressibility of water due to the presence of a methane molecule at a fixed position is measured by the excess isothermal compressibility[36,42] $\Delta\kappa_T = -\rho^0(\partial\Delta V/\partial P)_T$ that involves the density of pure water ρ^0 as well as the partial molar isothermal compressibility[21,76] $\mathcal{K}_T = -(\partial V_m/\partial P)_T$ described in SI. Our computed pressure dependence of excess isothermal compressibility is shown in the main plot of Figure 3 for $\Delta\kappa_T/\rho^0$ calculated using volume fluctuation and also by volume fitting. The fluctuation-calculated $\Delta\kappa_T/\rho^0$ values (filled circles) exhibit considerable scatter, with sampling uncertainties (not marked in the plot) larger than the maximum change in this quantity over the studied pressure. This result indicates that an accurate determination of compressibility by the volume fluctuation at a single pressure is currently beyond our reach. Sampling much more extensive than that used in the present study will be needed for such a determination in the future. Nonetheless, Figure 3 shows that the scatter of fluctuation-calculated $\Delta\kappa_T/\rho^0$ values are around the solid curve representing the $\Delta\kappa_T/\rho^0$ versus P function determined from volume fitting, indicating that even with limited sampling, the two methods did not produce inconsistent results. In our view, the general trend of the solid curve in the main plot of Figure 3 for $\Delta\kappa_T/\rho^0$ should be reliable because it was obtained with more underlying sampling from the derivative of a volume versus pressure function fitted from multiple pressures, a function that has small sampling uncertainties as shown by the error bars for the ΔV values in the inset of Figure 2. Indeed, the inset of Figure 2 demonstrates unequivocally that ΔV decreases with increasing P, hence $\Delta\kappa_T/\rho^0 > 0$. It also shows quite convincingly that the ΔV versus P curve concave upward, hence $\Delta\kappa_T/\rho^0$ decreases with increasing P (Figure 3). The partial molar isothermal compressibility $\mathcal{K}_T$ (dashed curve in Figure 3) follows a similar trend. Because κ_T^0 for pure water decreases with increasing pressure $(\partial\kappa_T^0/\partial P)_T < 0$), by eq S18, $\mathcal{K}_T$ (dashed curve) is always larger than $\Delta\kappa_T/\rho^0$ (solid curve). It should be noted that computational sampling performed for the present work was vastly more extensive than that feasible when the pressure-dependent compressibility results reported by our group in ref 42 were computed. Therefore, the present general predictions for the behavior of $\Delta\kappa_T/\rho^0$ and $\mathcal{K}_T$, namely, that both quantities are positive for $P = 1-3000$ atm and decrease with increasing P, should supersede the tentative interpretation in that earlier work (which were subjected to large sampling uncertainties) that $\Delta\kappa_T/\rho^0$ and $\mathcal{K}_T$ are negative at 1 atm and that both quantities increases with increasing pressure.[42]

The solid curve in Figure 3 shows that, according to our simulation, $\Delta\kappa_T/\rho^0 \approx 2.8 \times 10^{-3}$ Å^{3}atm^{-1} at $P = 1$ atm and $T = 298.15$ K. This value is much lower than the $\Delta\kappa_T/\rho^0 \approx (3.3 \pm 2.6) \times 10^{-3}$ atm^{-1} $\times$ 30 Å $\approx (0.1 \pm 0.08)$ Å^3 atm^{-1} value obtained by Matubayasi and Levy[36] at $T = 283.15$ K, where the $\rho^0 \approx 1/(30)$Å^3 value adopted here corresponds to the water density of 1 g cm^{-3} used in their calculation. Of relevance to the present and earlier[36] predictions of positive $\Delta\kappa_T/\rho^0$ values for methane is a recent study by Sarupria and Garde using SPC/E water around nonpolar solutes with radii ranging from ∼1 to 20 Å. These authors predicted that the isothermal compressibility of the hydration shell around the solute varies nonmonotonically with solute radius. For P = 1, 2000, and 3000 atm, hydration shell compressibility is higher than the compressibility of bulk water for solute radius $\gtrsim$5 Å but can be lower than the compressibility of bulk water for small solute radii,[43] suggesting that hydration shell compressibility is lower than bulk compressibility for a methane-sized solute. However, whether this result implies that the SPC/E model predicts negative $\Delta\kappa_T/\rho^0$ and $\mathcal{K}_T$ values remains to be elucidated.

Experimental data that can be compared directly with Figure 3 are limited. The experimental V_m values for methane in the inset of Figure 2 offer two estimates of $\mathcal{K}_T$ that differ by more than 1 order of magnitude: The difference between the V_m measured at 276.3 atm by Hnědkovský et al.[158] and the V_m measured at 1 atm by Masterton[120] leads to $\mathcal{K}_T \approx 1.2 \times 10^{-3}$ Å^3 atm^{-1} in the range of $P = 1-276.3$ atm (which is consistent with our simulation results in Figure 3); however, the difference between the two V_m values measured at 345.4 and 276.3 atm by Hnědkovský et al.[158] suggests a much higher $\mathcal{K}_T \approx 21.6 \times 10^{-3}$ Å^3 atm^{-1} in the range of $P = 276.3-345.4$ atm. Although a ∼20-fold increase in experimental $\mathcal{K}_T$ over ∼300 atm does not seem to be physically reasonable, this apparent disagreement between simulation and experiment deserves to be further investigated in the future. Nonetheless, both experimental $\mathcal{K}_T$ estimate are positive, which is consistent with our prediction but is in apparent contradiction to an early argument that "ice-like" water at a hydrophobic surface is less compressible than bulk water.[161,162] Because Figure 3 exhibits a decreasing $\mathcal{K}_T$ with increasing P, our simulation data do not support an increasing $\mathcal{K}_T$ with P, as suggested apparently by experimental measurements of partial molar adiabatic compressibilities of hydrophobic amino acids[163] (a trend that agrees fortuitously with an earlier tentative result based on limited sampling;[42] see above). However, a simplistic comparison between the pressure dependence of the partial molar adiabatic compressibilities of hydrophobic amino acids[163] with the partial molar isothermal compressibility of methane can be problematic because experimental and simulation data are lacking for converting adiabatic to isothermal partial molar compressibility at high pressures. Moreover, because of the prominent effects of the charged groups on compressibility, it may not be straightforward to decouple the pressure dependence of such effects from the total partial molar compressibility of the amino acid to arrive at a pressure-dependent partial molar compressibility for its nonpolar group.

It is instructive to compare our simulated $\mathcal{K}_T$ for methane with experimental data on the adiabatic compressibility contribution from an alanine side chain at P = 1 atm. Differences between adiabatic and isothermal partial molar compressibilities of a single methane at 1 atm can readily be determined from experimental or simulation data. Previous calculations by our group indicate that $\mathcal{K}_S \approx \mathcal{K}_T - 1.63 \times 10^{-3}$ Å^3 atm^{-1} and $\kappa_S/\rho^0 \approx \kappa_T/\rho^0 - 1.65 \times 10^{-3}$ Å^3 atm^{-1} at $T = 298.15$ K and 1 atm,[42] which means that the single-methane $\mathcal{K}_S$

dx.doi.org/10.1021/jp501935f | J. Phys. Chem. B 2014, 118, 7488−7509

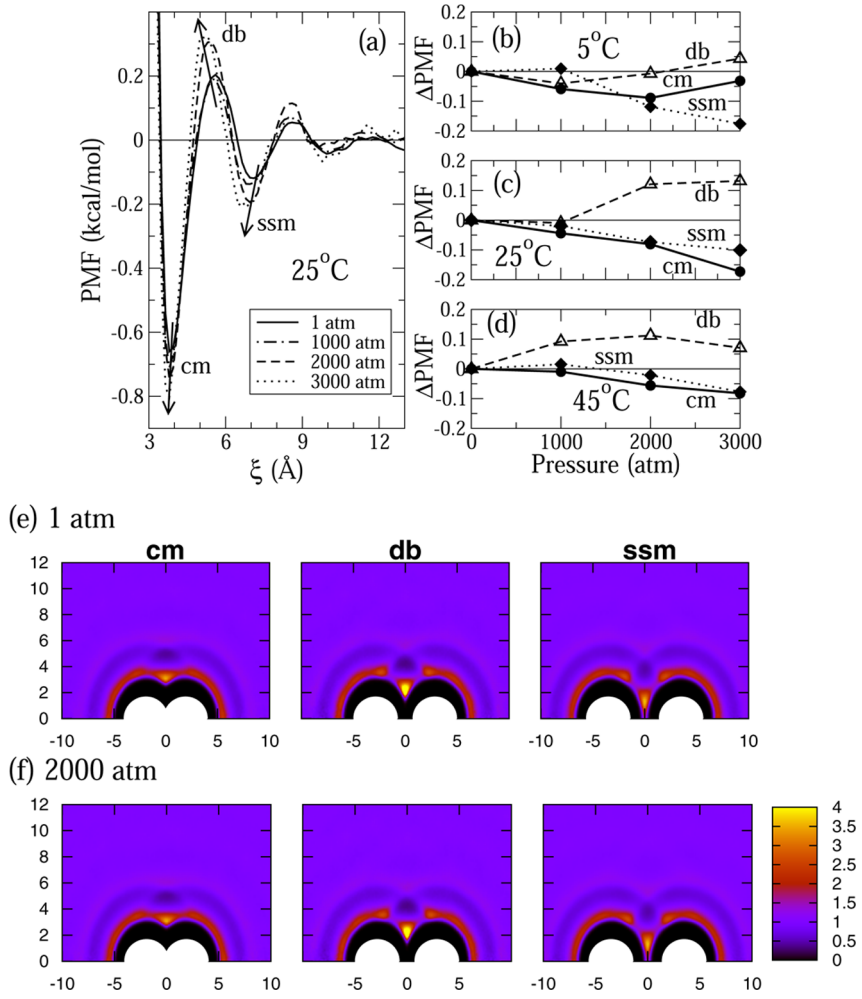

Figure 4. Pressure dependence of water-mediated hydrophobic interactions. (a) PMF of a pair methanes at T = 298.15 K (25 °C) and four different pressures. Direction of change in PMF value with increasing pressure P is indicated by arrows. There are small shifts in the cm, db, or ssm positions with increasing P. (b–d) P-dependent change in PMF. For each of the cm, db, and ssm configurations, ΔPMF at a given P is the PMF value at that P minus the corresponding PMF value at P = 1 atm and is given for (b) T = 278.15 K (5 °C), (c) 298.15 K (25 °C), and (d) 318.15 K (45 °C). (e–f) Density maps of water near a pair of methanes in the cm, db, and ssm configurations under (e) 1 atm and (f) 2000 atm. Density is given by $\rho_r(r,z)$ defined in eq S1 in SI; the horizontal scale (z) and vertical scale (r) are distance in Å. The white half circles represent the methanes. The color code on the right indicates relative density with unity corresponding to the bulk density for water molecules far away from the methanes.

and κ_S/ρ^0 predicted by the volume-fitting data in Figure 3 under the same conditions are 1.47×10^{-3} and 1.15×10^{-3} Å^3 atm^{-1} respectively. Experimental measurements of partial molar adiabatic compressibility of amino acids in water are negative[142,163−166] because of electrostriction caused by the charged amine and carboxyl groups.[167] Assuming group additivity, the contribution to partial molar adiabatic compressibility of an alanine side chain at 298.15 K and 1 atm has been estimated from the difference between the compressibilities of alanine and glycine[142,163−165] to be positive and ≈2.5×10^{-4} Å^3 atm^{-1}, which translates to a partial molar isothermal compressibility of $(2.5 \times 10^{-4} + 1.63 \times 10^{-3})$ Å^3 atm^{-1} = 1.88×10^{-3} Å^3 atm^{-1}. This estimate for an alanine side chain is about one-half (≈ 60%) of the $\mathcal{K}_T \approx 3.1 \times 10^{-3}$ Å^3 atm^{-1} we predicted for methane (Figure 3). Notably, for the same T,P conditions, the partial molar volume of alanine side chain estimated from the difference between alanine and glycine is 60.4−43.3 = 17.1 cm^3 mol^{-1} (ref 157) or ≈ 28 Å^3, which is also about one-half (≈ 45%) of the experimental $V_m \approx 62$ Å^3 for methane.[120] Interestingly, the experimentally measured compressibilities for valine, leucine, isoleucine, methionine, tyrosine, phenylalanine are more negative than that for alanine,[142,163−165] suggesting that compressibility contributions from multiple methylene groups or larger nonpolar groups can be negative at 298.15 K and 1 atm.[166,168] However, using an alternative Gly−X−Gly tripeptide approach and again assuming group additivity,[166,169] the partial molar adiabatic compressibility of an alanine side chain was estimated to be somewhat larger at approximately 6.2×10^{-4} Å^3 atm^{-1}, which translates to a partial molar isothermal compressibility of $(6.2 \times 10^{-4}+1.63 \times 10^{-3})$ Å^3 atm^{-1} = 2.55×10^{-3} Å^3 atm^{-1}, a value that is quite close to (≈ 73% of) our predicted $\mathcal{K}_T$ for methane at 298.15 K and 1 atm (Figure 3). In this case, the Gly−X−Gly estimated adiabatic compressibility contributions of larger hydrophobic side chain were found to be positive.[166]

C. PMF of Methane Pairs in Water. We now proceed to study the pressure and temperature dependence of water-mediated interactions between two methanes (Figure 4). Contact minimum (cm), desolvation barrier (db), and solvent (water)-separated minimum (ssm) are salient features of methane−methane PMFs (Figure 4a), as predicted theoretically[50] and verified by numerous subsequent numerical

dx.doi.org/10.1021/jp501935f | J. Phys. Chem. B 2014, 118, 7488−7509

simulations. At cm, the van der Waals surfaces of the two methanes overlap (white half circles in the left panels of Figure 4e,f). This configuration is favored (PMF < 0) because exposure of nonpolar surface to water is reduced relative to the situation when the two methanes are far apart (PMF = 0). At db, the van der Waals surfaces of the two methanes are not touching each other (middle panels of Figure 4e,f), thus the favorable van der Waals interactions between the methanes are partially lost but the space between the methanes is not large enough to accommodate water molecules (black area between the two methanes in the middle panels of Figure 4e,f) to make up for the loss in favorable contact energy. As a result, the db configuration is unfavorable (PMF > 0) relative to the cm configuration and also to configurations in which the two methanes are far apart. At ssm, the two methanes are just sufficiently far apart that water molecules in contact with both methanes can be accommodated between them (blue and red areas between the methanes in the right panels of Figure 4e,f). Water molecules associated with this two-methane configurations provide a small yet robust stabilization[50] that leads to slightly favorable PMF values at ssm.

The PMFs at 298.15 K show that as pressure increases, both cm and ssm deepen. The stabilization of cm by pressure is consistent with a recent scaled particle theory analysis.[170] In contrast, db becomes higher (more unfavorable) as pressure increases. The trends for 298.15 K are shown in Figure 4c. The corresponding trends of PMF values at cm, db, and ssm for 278.15 and 318.15 K are reported, respectively, in Figure 4b,d. Pressure dependence of PMF is temperature sensitive. For instance, P-variation of cm is nonmonotonic at 278.15 K (cm increases, or destabilizes, at high P in Figure 4b), but is monotonically decreasing (stabilized by P) for 298.15 and 318.15 K (Figure 4c,d). Another example is that db increases monotonically from P = 1000 to 3000 atm at 278.15 and 298.15 K (Figure 4b,c) but decreases from P = 2000 to 3000 atm at 318.15 K (Figure 4d). The molecular basis for the peculiar trends at T = 278.15, including the stabilization of ssm relative to cm from P = 2000 to 3000 atm (not observed for 298.15 K and 318.15K) is beyond the scope of our present investigation and needs to be addressed in the future.

As far as our results for T = 298.15 K are concerned, they are in large measure—though not entirely[170]—consistent with those obtained by Hummer et al. using 256 SPC waters and information theory at 298 K[38] and by Ghosh et al. using a system of 10 methanes with 508 TIP3P waters at 300 K.[40] A notable exception, however, is that although they both predicted increasing stabilization of ssm relative to cm as pressure increases, Figure 4c shows that cm decreases faster than ssm between P = 2000 and 3000 atm at 298.15 K. In Figure 5, we summarize the presently predicted temperature and pressure dependence of the relative stabilities between db and cm (which may be viewed as a solvation barrier), between ssm and cm, and between db and ssm.

The density plots in Figure 4e,f show that water density is significantly higher at the first hydration shell around the methanes (deep red areas), especially the region in between the two methane (yellow spots). Water density is also slightly enhanced at the second hydration shell (faintly red areas), whereas water density is reduced between the first and second hydration shells (deep blue areas). These patterns are expected from standard radial distribution function analyses.[50] The region of maximum water density (bright yellow spot) moves progressively closer to the midpoint between the two methanes

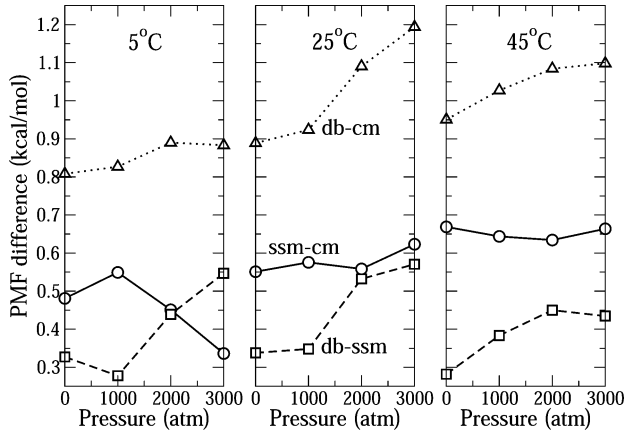

Figure 5. Pressure and temperature dependence of barrier heights and local minimum depths in the two-methane PMF. The ξ_1-ξ_2 notation "db-cm" (triangles), "ssm-cm" (circles), and "db-ssm" (squares) denotes [(PMF value at ξ_1) minus (PMF value at ξ_2)]. For instance, db-cm is the PMF value at the desolvation barrier (db) minus the PMF value at the contact minimum (cm). The dotted, solid, and dashed lines are merely guides for the eye.

as ξ increases from cm to db to ssm. However, even for the ssm configuration, the region of maximum water density does not lie along the line directly connecting the two methanes. Instead, it is approximately 1 Å away from that line. In three dimensions, this region takes the shape of a ring of radius ≈1 Å centered at the midpoint and perpendicular to the line between the two methanes, as has been observed in the simulation by Ghosh et al.[41] Difference in water density distribution between P = 1 and 2000 atm is subtle and not clearly discernible from visual comparison of Figure 4e and Figure 4f. We also note that Figure 4e,f does not exhibit prominent ripple-like patterns as those featured in the corresponding density plots for a two-dimensional water model.[171]

The pressure dependence of enthalpic and entropic contributions to two-methane PMF (Figure 6) was determined using eq S5 in SI. Because the model methane molecules have no internal degrees of freedom, the entropic contributions originate entirely from the water molecules. Pressure−volume ($P\Delta V$) contribution is negligible at P = 1 atm, but its contribution to ΔH is appreciable at high P (Figure 6f). Enthalpy−entropy compensation is prevalent (Figure 6a,b). This behavior is akin to similar compensations observed before at P = 1 atm[27,105] as well as at 4000 atm.[41] Overall, the general trend of pressure-dependent enthalpic and entropic properties in Figure 6a,b is consistent with that in the early study of Ghosh et al.[41] Figure 6c shows that db is made more unfavorable by pressure due to entropic effects. Enthalpic effects at db is apparently pressure-neutral between 1 and 3000 atm (Figure 6d). Further decomposition of the enthalpic contribution at db indicates that as pressure increases, there is a compensation between a stabilizing energy (lower ΔE near db at P = 3000 atm in Figure 6e) and a destabilizing pressure−volume term (positive $P\Delta V$ near db in Figure 6f). In contrast, Figure 6d shows that as pressure increases, ssm is stabilized by enthalpy whereas the entropic effects near ssm is essentially pressure-neutral (Figure 6c). Further decomposition of the pressure-induced decrease in ΔH around ssm indicates that ssm is favored by both negative values of ΔE (Figure 6e) and $P\Delta V$ (Figure 6f).

dx.doi.org/10.1021/jp501935f | J. Phys. Chem. B 2014, 118, 7488−7509

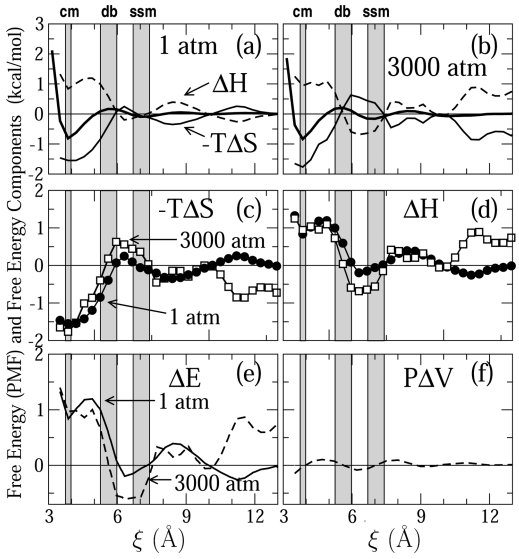

Figure 6. Pressure dependence of the enthalpic and entropic components of two-methane PMF at T = 298.15 K. Shaded vertical bands show the ranges of cm, db, and ssm positions for the range of P we simulated (see Figure 4a). (a,b) PMF (thick solid curves) and its enthalpic component (ΔH, dashed curves) and entropic component ($-T\Delta S$, thin solid curves) at pressure P = 1 atm (a) and 3000 atm (b). (c,d) Comparison of the entropic (c) and enthalpic (d) PMF components at these two pressures. Data for P = 1 and 3000 atm are shown by the filled and open symbols, respectively. (e,f) The enthalpic PMF components ΔH are further decomposed into their respective energetic [ΔE, (e)] and pressure–volume [$P\Delta V$, (f)] contributions. Data for P = 1 and 3000 atm are shown by the solid and dashed curves, respectively. The $P\Delta V$ contribution at 1 atm is so small that its deviation from zero is indiscernible in (f).

D. Volume of Methane Pairs in Water. The average volumes of model systems consisting of a pair of methanes embedded in N = 746 water molecules are shown in Figure 7 for the four different pressures considered in this study. We denote this average volume by $\langle V(\xi)\rangle_{N,ab}$ as its value is dependent upon the distance ξ between the two methanes (symbolized by a and b). Figure 7 shows that spatial dependence is strongly oscillatory for all pressures studied with a prominent peak near db (4.5 Å < ξ < 6 Å) and a deep minimum near ssm (6.5 Å < ξ < 7.5 Å). The overall increase in volume near db is related to the steric impossibility of accommodating water molecules in the space between the two methanes, as discussed above, leading to a void volume that adds to the overall volume. Not surprisingly, the ξ-dependent oscillation of volume is suppressed by pressure. For instance, the difference between the volume at db and at ssm is 8.78 Å^3 at 1 atm but only 4.30 Å^3 at 3000 atm.

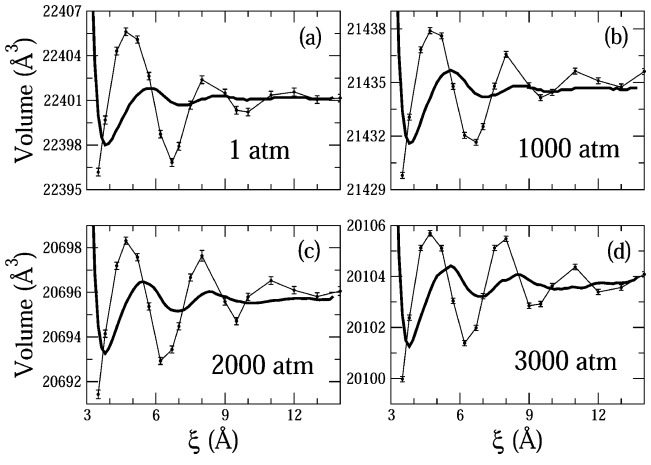

Figure 7. Average volume ($\langle V(\xi)\rangle_{N,ab}$) at T = 298.15 K of the two methanes plus water system as a function of methane–methane separation ξ. Volume data points are shown with error bars determined using block averages. Lines joining data points are merely guides for the eye. As position references, the two-methane PMFs for the respective pressures (continuous curves, data from Figure 4a) are shown in an arbitrary vertical scale.

The average volume $\langle V(\xi)\rangle_{N,ab}$ at very large methane–methane distances ($\xi \to \infty$) is expected physically to be equal to the volume of a box containing two isolated methanes embedded in the same number N of water molecules, that is, $\langle V(\xi \to \infty)\rangle_{N,ab} = 2\langle V\rangle_{N,a} - \langle V\rangle_N$. Equivalently, $\langle V(\xi \to \infty)\rangle_{N,ab}$ may be understood as the sum of the volume of N water molecules plus two times the excess volume $\langle V\rangle_{N,a} - \langle V\rangle_N$ for a single methane. Now we use $\langle V(\xi \to \infty)\rangle_{N,ab}$ as reference volume to define a ξ-dependent excess volume of two-methane association, viz. (Figure 8a)

$$\Delta V(\xi) \equiv \langle V(\xi)\rangle_{N,ab} - \langle V(\xi \to \infty)\rangle_{N,ab} \quad (1)$$

In Figure 8a, even at the largest methane–methane distance simulated (14 Å), the methanes are not sufficiently far apart to mimic infinite separation. But this lack of convergence [i.e., $\Delta V(\xi = 14\ \text{Å}) \neq 0$] is not expected to affect the accuracy of the $\Delta V(\xi)$ values at smaller ξ because each $\Delta V(\xi)$ data point was computed independently and even at ξ = 10 Å, a spatial separation of $\gtrsim$24 Å or more than eight layers of water molecules are available to screen a methane from the periodic-boundary-conditions effect of the other methane.

Figure 8b shows a clear trend of ΔV reduction near db with increasing P—this applies to the db position at P = 1 atm as well as the positions for peak ΔV values at various Ps, indicating positive excess compressibility around the db configuration. In line with intuition, this observation suggests that the db-associated void volume between the two methanes decreases with increasing pressure. However, surprisingly, ΔV near ssm—including the ssm position at P = 1 atm as well as the positions for the first local minimum ΔV values at various Ps—increases with increasing pressure. This observation implies that, relative to configurations with the two methanes far apart, the system at methane–methane distances between 6.5 and 7.5 Å packs even more tightly at low pressures than at higher pressures. Figure 8b shows further that at high pressure, system volume at cm is smaller than that at large ξ and also smaller than that at ssm. This finding suggests that in the TIP4P water model, the cm-type of partially exposed two-methane configurations are more favorable at high pressure (2000–3000 atm) than the ssm-type of more water-exposed configurations. Notable changes in ΔV are also observed at distances corresponding to the second solvent-separated configuration (i.e., distances where approximately two layers of water molecules are separating the two methanes). The volume at these configurations decreases with increasing pressure and becomes smaller than the reference $\xi \to \infty$ volume for P > 2000 atm.

As discussed above, an intuitively physical origin for the ΔV peak near db is the void volume created by the two methanes at distances between ~4–6 Å. Here we examine this idea quantitatively by comparing the explicit-water-simulated volume peaks with analytically determined volumes encased

dx.doi.org/10.1021/jp501935f | J. Phys. Chem. B 2014, 118, 7488–7509

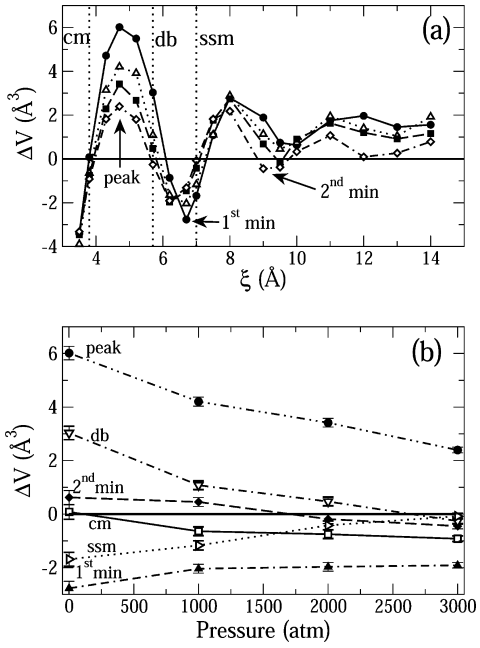

Figure 8. Volume effect of methane association in water at T = 298.15 K. The distance-dependent two-methane $\Delta V(\xi)$ is defined in the text. (a) $\Delta V(\xi)$ values for P = 1, 1000, 2000, and 3000 atm are given by the filled circles, open triangles, filled squares, and open diamonds, respectively. As a guide for the eye, these data points are connected by solid, dotted, dashed, and dashed-dotted lines, respectively. The ΔV profiles at different pressures share the prominent features of a peak, a first minimum, and a second minimum. As position references, the cm, db, and ssm positions of the PMF at P = 1 atm are marked by vertical dotted lines. (b) Pressure dependence of the volume change ΔV at the peak, first minimum, and second minimum value for each of the given pressure as well as at the cm, db, and ssm positions marked in (a).

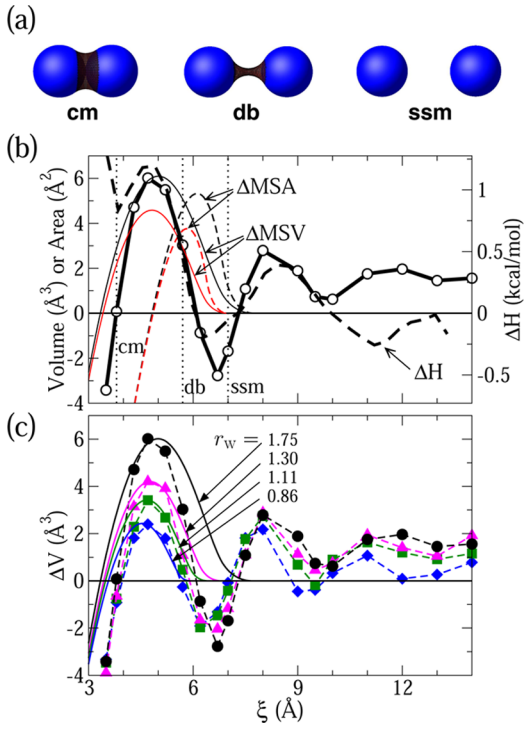

Figure 9. Rationalization of excess volumes of two-methane association by analytically constructed molecular surfaces. Here simulated $\Delta V(\xi)$ for two methanes (Figure 8a) at T = 298.15 K is compared with ξ-dependent variation of the area of the two-methane molecular surface (ΔMSA) and of the volume ΔMSV encased by the two-methane molecular surface. The radius of the molecular surface of a single methane is taken to be R = 2.09 Å. (a) Molecular surfaces of a pair of methanes at cm, db, and ssm. These positions are marked in (b) by vertical dotted lines. The molecular surfaces in (a) are defined by a water probe with radius r_w = 1.77 Å.[172,173] When a water probe can be accommodated between the two methanes, as for the ssm, the molecular surface is the union of the disjoint surfaces of the two methanes (blue surfaces). When the two methanes are at closer distances, the molecular surface is contiguous, as for the cm and db. For these positions, the molecular surface of the methane pair consists of the exposed blue surfaces of the methanes as well as the black translucent surfaces between the methanes. (b) Contrasting the simulated ξ-dependent excess volume $\Delta V(\xi)$ in Figure 8a for P = 1 atm (open circles connected by thick continuous black curve) with the ξ-dependent molecular surface volume (ΔMSV) calculated using eqs 5−7 with water probe radius r_w = 1.77 Å (thin continuous black curve) or r_w = 1.4 Å (thin continuous red curve). The corresponding ξ-dependent molecular surface area (ΔMSA; eqs 2−4) are also included for comparison (thin dashed black and red curves, respectively, for ΔMSA calculated using r_w = 1.77 Å and r_w = 1.4 Å). Units for volume and area are provided by the left vertical scale. Also included for comparison is the enthalpic component ΔH of the two-methane PMF for P = 1 atm. The units for ΔH is provided by the right vertical scale. This plot shows that the peak position of two-methane excess volume ΔV coincides almost exactly with the peak position of enthalpic PMF near the db position, thus suggesting strongly that the void volume developed between the two methanes around the db because of steric dewetting and the associated loss of favorable intermolecular interaction is a major origin of the enthalpic barrier.[105] (c) Simulated two-methane excess volume $\Delta V(\xi)$ for P = 1, 1000, 2000, and 3000 atm (black circles, magenta triangles, green squares, and blue diamonds, respectively, data points connected by dashed curves in the same color) are compared against the best-fit ΔMSV using different optimal r_w values for different pressures (continuous curves in corresponding colors).

by molecular surfaces that are defined by water probes of various sizes (Figure 9). Molecular surface[172] of a group of molecules, also referred to as Connolly surface,[173] is defined as the union of all the contact surfaces plus all the reentrant surfaces between a spherical probe of a given size and the group of molecules under consideration. For a water-sized probe, the probe radius r_w is often taken to be 1.4 Å.[173] Molecular surface is related to but distinct from solvent-accessible surface.[174] Because solvent-accessible surface is defined as the surface traced by the center of a spherical probe in contact with the group of molecules in question rather than the contact points on the probe, the volume encased by solvent-accessible surface is generally larger than that encased by molecular surface. Molecular surface area (MSA) and solvent-accessible surface area (SASA) are useful for understanding different aspects of solvation effects.[105,172] Notably, the db of pairwise methane PMF is rationalized by a local maximum in MSA as the two methanes approach each other (Figure 9a), but SASA decreases monotonically with decreasing ξ and thus exhibits no local barrier for two methanes.[25,92]

For two hard spheres with radius R and their centers at a distance ξ apart, the ξ-dependent MSA defined by a probe of radius r_w relative to the corresponding MSA for two independent hard spheres (i.e., at large ξ) is given by

dx.doi.org/10.1021/jp501935f | J. Phys. Chem. B 2014, 118, 7488−7509

$$\Delta\mathrm{MSA}(\xi) = \begin{cases} \Delta\mathrm{MSA}_1(\xi), & \text{if } 0 \le \xi < 2\sqrt{R(R+2r_w)}; \\ \Delta\mathrm{MSA}_2(\xi), & \text{if } 2\sqrt{R(R+2r_w)} \le \xi < 2(R+r_w); \\ 0, & \text{if } \xi \ge 2(R+r_w) \end{cases} \quad (2)$$

where

$$\Delta\mathrm{MSA}_1(\xi) = 4\pi\{(R^2 - r_w^2)\lambda_1/r_w - R^2 + r_w x_0 \sin^{-1}(\lambda_1/r_w)\} \quad (3)$$

$$\Delta\mathrm{MSA}_2(\xi) = 4\pi\{(R^2 - r_w^2)\lambda_1/r_w - R^2 + r_w x_0[\sin^{-1}(\lambda_1/r_w) - \sin^{-1}(\lambda_2/r_w)] + r_w\lambda_2\} \quad (4)$$

$x_0 = x_0(\xi) \equiv [(R + r_w)^2 - \xi^2/4]^{1/2}$, $\lambda_1 = \lambda_1(\xi) \equiv r_w\xi/[2(R + r_w)]$, and $\lambda_2 = \lambda_2(\xi) \equiv [(\xi^2/4) - R(R + 2r_w)]^{1/2}$. The above expression for $\Delta\mathrm{MSA}(\xi)$ is equivalent to the quantity $M_A(x) - 8\pi R_s^2$ derived by Rank and Baker,[92] where their variables x and R_s correspond to our variables ξ and R, respectively.

After performing the pertinent volume integrals for the above-defined two-sphere system, we arrived at the following formula for the ξ-dependent volume encased by the molecular surface relative to the total volume of two independent hard spheres of radius R:

$$\Delta\mathrm{MSV}(\xi) = \begin{cases} \Delta\mathrm{MSV}_1(\xi), & \text{if } 0 \le \xi < 2\sqrt{R(R+2r_w)}; \\ \Delta\mathrm{MSV}_2(\xi), & \text{if } 2\sqrt{R(R+2r_w)} \le \xi < 2(R+r_w); \\ 0, & \text{if } \xi \ge 2(R+r_w) \end{cases} \quad (5)$$

where

$$\Delta\mathrm{MSV}_1(\xi) = 2\pi\{\lambda_1(x_0^2 + r_w^2 - x_0\sqrt{r_w^2 - \lambda_1^2}) - \lambda_1^3/3 - x_0 r_w^2 \sin^{-1}(\lambda_1/r_w) - R^3[2 - 3\lambda_1/r_w + (\lambda_1/r)^3]/3\} \quad (6)$$

$$\Delta\mathrm{MSV}_2(\xi) = 2\pi\{(\lambda_1 - \lambda_2)(x_0^2 + r_w^2) - x_0(\lambda_1\sqrt{r_w^2 - \lambda_1^2} - \lambda_2\sqrt{r_w^2 - \lambda_2^2}) - (\lambda_1^3 - \lambda_2^3)/3 - x_0 r_w^2[\sin^{-1}(\lambda_1/r_w) - \sin^{-1}(\lambda_2/r_w)] - R^3[2 - 3\lambda_1/r_w + (\lambda_1/r)^3]/3\} \quad (7)$$

The relative molecular-surface volume $\Delta\mathrm{MSV}(\xi)$ for a pair methane-sized hard spheres is shown in Figure 9b for two different probe radii. The plot shows that $\Delta\mathrm{MSV}(\xi)$ (thin solid curves) provides a reasonable rationalization for the db-associated explicit-water-simulated ΔV peak, even though $\Delta\mathrm{MSV}(\xi)$ does not account for the negative ΔV values near ssm. For both probe radii tested, $\Delta\mathrm{MSV}(\xi)$ peaks at $\xi \approx 4.5$–5.0 Å, essentially coinciding with the peak ΔV position at $P = 1$ atm. In contrast, the $\Delta\mathrm{MSA}(\xi)$ area functions peak at a slightly larger distance ~6 Å which is nearer to the db position. The enthalpy function $\Delta H(\xi)$ here (dashed black curve) is seen to track $\Delta\mathrm{MSV}(\xi)$ closely, achieving its peak value near the ΔV peak at a distance ξ that is slightly smaller than that for the PMF db peak. This behaviorial pattern may be quite general as a similar relationship between the db position and the peak positions of ΔH and ΔV was observed for a pair of polyalanine α-helices.[105]

Notably, Figure 9b indicates that the peak ΔV value for $P = 1$ atm is reproduced by the $\Delta\mathrm{MSV}$ for $r_w \approx 1.77$ Å (thin solid black curve) rather than the $\Delta\mathrm{MSV}$ for the commonly used $r_w = 1.4$ Å water-sized probe (thin red curve). Figure 9c shows further that peak ΔV values simulated at different pressures can be reproduced by $\Delta\mathrm{MSV}$ with different probe sizes. In this respect, it has been noted that the average separation between a water molecule and different parts of a solute surface can vary in general, thus the utility of using exclusively a fixed-radius water probe can be limited.[175,176] The qualitative trend of a decreasing water probe size with increasing pressure in Figure 9c is consistent with expectation. Quantitatively, however, the probe size derived from fitting the ΔV peak at high pressure is probably too small to represent a real water molecule. A case in point is that whereas density of pure water increases by only ~10% from 1 to 3000 atm[42] (hence ~10% decrease in volume), the best-fit r_w at 3000 atm in Figure 9c is ~1/2 that at 1 atm, which translates to >80% decrease in volume. This mismatch suggests that for configurations around the ΔV peak, the relatively small peak ΔV values under high pressures likely originate from a partial compensation of the db-associated void by volume-decreasing effects of significantly higher-than-bulk water densities in surrounding regions.

E. Compressibility Effects of Methane–Methane Association in Water. The combined effect of pressure and spatial proximity of two methanes on the overall compressibility of the aqueous methane system is provided in Figure 10. The plotted quantity

$$(\kappa_T)_{N,ab}(\xi) = -\frac{1}{\langle V(\xi)\rangle_{N,ab}}\left(\frac{\partial\langle V(\xi)\rangle_{N,ab}}{\partial P}\right)_T \quad (8)$$

is the isothermal compressibility derived from the average volume $\langle V(\xi)\rangle_{N,ab}$ in Figure 7. As in our consideration above of a single methane, two-methane compressibility at a given ξ is estimated here using two independent methods: by volume fluctuation at a single pressure or by differentiating the pressure dependence of volume fitted over multiple pressures using functions quadratic in P. The methods are basically identical to those we used above for the compressibility of a single methane in water, the only extension here is that we now apply the methods for each and every methane–methane distance ξ we consider.

Notwithstanding the large numerical uncertainties (see discussion in SI) and thus the tentative nature of the present compressibility results, because two independent methods were used to estimate $(\kappa_T)_{N,ab}(\xi)$, there is no reason for potential biases that afflict one method to also afflict the other method. Moreover, because data at different ξ positions were collected independently of one another in our approach, there is no a priori correlation between data at different ξs. Taking these considerations together, it is reasonable to expect that robust features common to the $(\kappa_T)_{N,ab}(\xi)$ obtained by both methods are likely valid predictions of the underlying methane plus water model. We focus on those features below.

At each of the four pressures in Figure 10, a local maximum in $(\kappa_T)_{N,ab}(\xi)$ occurs near db, and a local minimum presents itself near ssm. This trend is reasonable because the low density (high ΔV, see dashed curves in Figure 10) around db is likely conducive to a higher compressibility, and conversely, the high

dx.doi.org/10.1021/jp501935f | J. Phys. Chem. B 2014, 118, 7488–7509

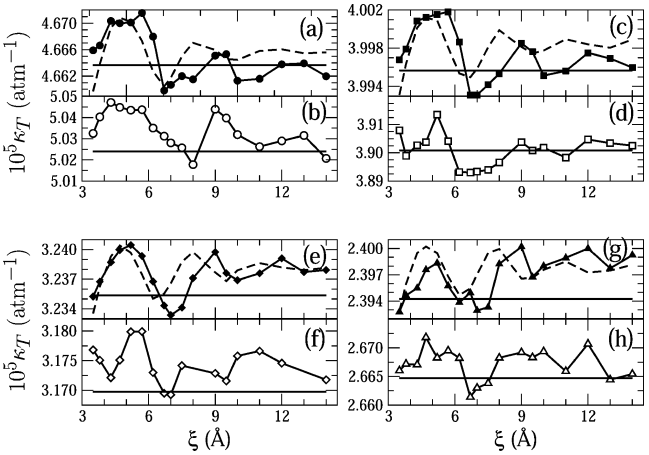

Figure 10. Isothermal compressibility of a pair of methanes in water at T = 298.15 K. $(\kappa_T)_{N,ab}$ of the two methanes plus water system was computed from pressure derivatives of fitted volumes [filled symbols in (a), (c), (e), (g)] and from volume fluctuations at the given pressure [open symbols in (b), (d), (f), (h)] for P = 1 atm (a,b), 1000 atm (c,d), 2000 atm (e,f), and 3000 atm (g,h). For comparison, the horizontal lines provide the compressibility $(\kappa_T)_{N,a}$ of the single methane plus water system computed using the method for the given panel (data from Figure 3). The corresponding ξ-dependent average volume is also shown as position reference (dashed curves, data from Figure 7 plotted in arbitrary vertical scales).

density (low ΔV, see dashed curves in Figure 10) around ssm is suggestive of a lower compressibility. Interestingly, the two-methane isothermal compressibilities around ssm for all four pressures are lower than the corresponding one-methane isothermal compressibility (marked by horizontal lines in Figure 10). Because the immersion of a methane molecule in water increases the isothermal compressibility of the system (Figure 3), one might expect that introducing a second methane would increase isothermal compressibility even further. However, this is not the case around ssm, underscoring the exceptionally well-packed nature of water in the vicinity of such methane configurations.

As in our examination of $\Delta V(\xi)$ above, it is useful to consider the isothermal compressibility of a pair of methanes at a distance ξ in water relative to the isothermal compressibility when the two methanes are far apart. Here we refer to this quantity

$$\Delta\kappa_T(\xi) \equiv -\rho^0\left(\frac{\partial\Delta V(\xi)}{\partial P}\right)_T \qquad (9)$$

as the two-methane excess isothermal compressibility. Figure 11a shows the pressure dependence of $\Delta\kappa_T(\xi)/\rho^0$. According to eq 9, $\lim_{\xi\to\infty}\Delta\kappa_T(\xi) = 0$ because $\lim_{\xi\to\infty}\Delta V(\xi) = 0$ (eq 1). However, because $\Delta V(\xi) \neq 0$ at the largest distance ξ = 14 Å simulated (i.e., 14 Å is not sufficiently large for $\xi \to \infty$ behaviors; see Figure 8a), $\Delta\kappa_T(\xi$ = 14 Å) $\neq 0$ (Figure 11a). Nonetheless, for the same reasons given in the discussion of $\Delta V(\xi)$, we do not expect the nonzero $\Delta\kappa_T(\xi)$ values at ξ = 14 Å to impact upon the accuracy of $\Delta\kappa_T(\xi)$ values at smaller ξ.

Figure 11a shows that the largest variations in simulated ξ-dependent $\Delta\kappa_T(\xi)/\rho^0$ values at P = 1 atm are $\approx +1.8 \times 10^{-3}$ Å^3 atm^{-1} and -1.2×10^{-3} Å^3 atm^{-1} in the positive and negative directions, respectively. These variations are of the same order of magnitude as the simulated single-methane $\Delta\kappa_T/\rho^0 \approx 2.8 \times 10^{-3}$ Å^3 atm^{-1} reported above for P = 1 atm. It follows that the simulated partial molar isothermal compressibility of a pair of methanes in water ranges approximately from $(2 \times 2.8-1.2) \times 10^{-3} = 4.4 \times 10^{-3}$ Å^{3}atm^{-1} to $(2 \times 2.8 + 1.8) \times 10^{-3} = 7.4 \times 10^{-3}$ Å^3 atm^{-1}. These values are ≈0.86−1.45 times the experimental partial molar isothermal compressibility of two independent alanine side chains, which was estimated to be ≈2 × 2.55 × 10^{-3} = 5.1 × 10^{-3} Å^3 atm^{-1} from Gly−X−Gly tripeptide data.[166] This approximate agreement is reassuring, although it is not a direct comparison between simulation and experiment because experimental data on the compressibility of a pair of methanes in water are lacking.

The favorable comparison above between simulation and experiment suggests that the present computational results on compressibility are physically reasonable despite limited sampling (see SI). Several salient trends in our results are noteworthy. Figure 11 suggests that $\Delta\kappa_T(\xi)$ decreases with

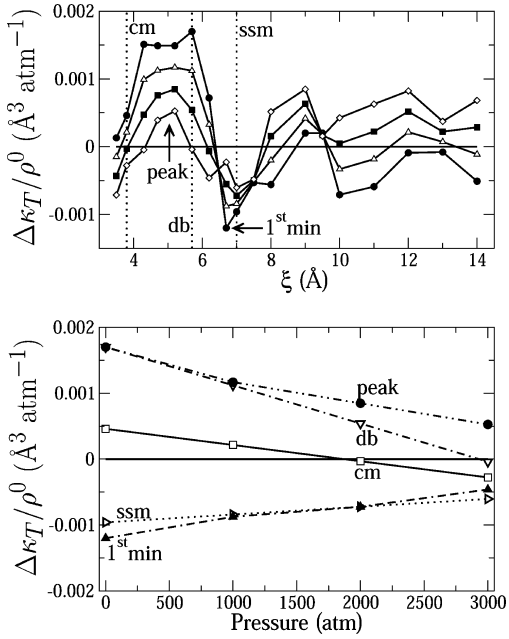

Figure 11. Excess isothermal compressibility of a pair of methanes in water at T = 298.15 K. (a) $\Delta\kappa_T/\rho^0$ is two-methane excess compressibility divided by the density of pure water, shown as a function of methane−methane separation for pressure P = 1 atm (filled circles), 1000 atm (open triangles), 2000 atm (filled squares), and 3000 atm (open diamonds). The compressibilties used to compute the excess compressibilities here (eq 9) were determined using pressure derivatives of fitted volumes (Figure 10a, c, e, and g). The cm, db, and ssm positions at P = 1 are marked by vertical dotted lines as position references. (b) Pressure dependence of the $\Delta\kappa_T/\rho^0$ values at the cm, db, and ssm, as well as the "peak" and "1st min" positions marked in (a). Note that the ξ coordinates for the "peak" and "1st min" positions can be different for different pressures.

increasing pressure around cm and db but increases around ssm. As a result of a decreasing trend of $\Delta\kappa_T$ with pressure at cm, excess isothermal compressibility at cm is seen as positive for $P \lesssim 2000$ atm but becomes slightly negative for $P \gtrsim 2000$ atm in Figure 11. In contrast, excess isothermal compressibility at the $\Delta\kappa_T$ peak near db is positive for all pressures we studied, even though $\Delta\kappa_T$ at this position also decreases with pressure. At ssm and the local $\Delta\kappa_T(\xi)$ minimum nearby, $\Delta\kappa_T(\xi)$ is negative for the pressures studied, but it becomes less negative as pressure increases. A possible physical reason for these trends is that as the water becomes more densely packed by

dx.doi.org/10.1021/jp501935f | J. Phys. Chem. B 2014, 118, 7488−7509

pressure, there is less room for fluctuation in water density around the two methanes. Such a reduction in the variation of water density may underlie the apparent convergence of $\Delta\kappa_T$ values, irrespective of ξ, to the same essentially zero value as pressure increases (Figure 11b). At ssm, an increase in $\Delta\kappa_T$, or more precisely, a decrease in the magnitude of negative $\Delta\kappa_T$ value with increasing pressure from 1 to 3000 atm, may also reflect that more water can be squeezed by an increasing pressure into the accessible yet largely unfavorable volume directly in between the two methanes (see the rightmost ssm panels in Figure 4e,f) and thus make the system more compressible. Nevertheless, while we believe that this line of reasoning is physically plausible, more extensive simulations and in-depth analysis will be needed to elucidate the molecular basis of the pressure dependence trends seen in Figure 11.

In view of the many experiments that measure adiabatic (isentropic)[142,163−166] rather than isothermal compressibilities, we consider also the ξ-dependent two-methane excess adiabatic compressibility, $\Delta\kappa_S(\xi)$, which is related to the excess isothermal compressibility $\Delta\kappa_T(\xi)$ by

$$\Delta\kappa_S(\xi)/\rho^0 = \Delta\kappa_T(\xi)/\rho^0 + T\left(\frac{\alpha^0}{\rho^0 C_P^0}\right)^2 \Delta C_P(\xi) - 2T\left(\frac{\alpha^0}{\rho^0 C_P^0}\right)\left(\frac{\partial \Delta V(\xi)}{\partial T}\right)_P \quad (10)$$

The above equation is a straightforward extension of the corresponding formula linking excess adiabatic and isothermal compressibilities for a single solute.[42,76,177] As in ref 42, ρ^0, α^0, and C_P^0 are, respectively, density, constant-pressure expansivity, and constant-pressure heat capacity of pure water. Here, $\Delta C_P(\xi)$ is the ξ-dependent constant-pressure excess heat capacity, and $(\partial\Delta V(\xi)/\partial T)_P$ is proportional to the ξ-dependent constant-pressure excess expansivity for a pair of methanes in water. To arrive at an estimate of two-methane excess adiabatic compressibility for T = 298.15 K and P = 1 atm (Figure 12), we use experimental data for the pure-water quantities under these conditions[147] (summarized in Table 1 of ref 42), namely, ρ^0 = 0.0553 mol cm^{-3}, $\alpha^0 = 2.57 \times 10^{-4}$ K^{-1}, and C_P^0 = 75.3 J mol^{-1} K^{-1}. As two-methane data are not available experimentally, to complete the analysis, we apply the $\Delta C_P(\xi)$ simulated previously by Shimizu and Chan[31] as well as a $(\partial\Delta V(\xi)/\partial T)_P$ function estimated from our present simulations of ξ-dependent excess volume at three different temperatures (Figure 12a). The resulting excess adiabatic compressibilities $\Delta\kappa_S(\xi)/\rho^0$ in Figure 12b (dashed curves) exhibit trends that are very similar to the corresponding excess isothermal compressibilities $\Delta\kappa_T(\xi)/\rho^0$ (solid curves in Figure 12b). As for $\Delta\kappa_T(\xi)/\rho^0$, a peak value around db and a local minimum around ssm are salient features of the adiabatic $\Delta\kappa_S(\xi)/\rho^0$.

We view the $\Delta\kappa_S(\xi)/\rho^0$ determined by fitting multiple-P data as more reliable than that calculated using volume fluctuation at a single P (see discussion on single-methane compressibility above). For this $\Delta\kappa_S(\xi)/\rho^0$ function (bottom dashed curve in Figure 12b), the maximum ξ-dependent variations in the positive and negative directions are $\approx +0.8 \times 10^{-3}$ and -1.1×10^{-3} Å^3 atm^{-1} respectively. Because the simulated excess adiabatic compressibility $\Delta\kappa_S/\rho^0$ of a single methane is $\approx$1.15 $\times 10^{-3}$ Å^3 atm^{-1}, the ξ-dependent values in Figure 12b imply that the partial molar adiabatic compressibility of a pair of methanes in water ranges approximately from 1.2×10^{-3} to 3.1×10^{-3} Å^3 atm^{-1} (because $2 \times 1.15 - 1.1 = 1.2$ and $2 \times 1.15 + 0.8 = 3.1$).

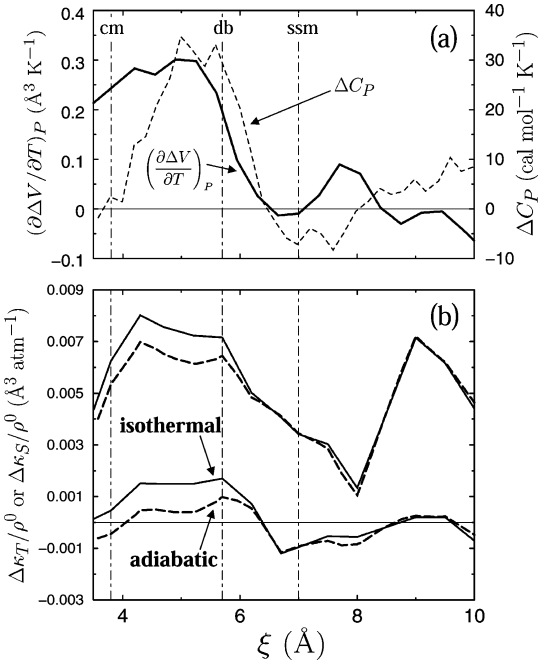

Figure 12. Excess adiabatic compressibility of a pair of methanes in water at T = 298.15 K and P = 1 atm, where $\Delta\kappa_T/\rho^0 = (\partial\Delta V(\xi)/\partial P)_T$ and $\Delta V(\xi)$ is the two-methane excess volume provided in Figure 8a. The cm, db, and ssm positions of the PMF are marked by vertical dashed-dotted lines. (a) Quantities needed for converting isothermal compressibility to adiabatic compressibility [eq 10]. Two-methane $(\partial\Delta V/\partial T)_P$ at 298.15 K (solid curve, left vertical scale) was derived using a quadratic T-dependent fit of simulated two-methane excess volume for P = 1 atm at 278.15, 298.15, and 318.15 K. Two-methane ΔC_P at 298.15 K and P = 1 atm (dashed curve, right vertical scale) was taken from Figure 4B of Shimizu and Chan.[31] (b) Excess adiabatic compressibility divided by density of pure water ($\Delta\kappa_S/\rho^0$, dashed curves) was derived from the simulated excess isothermal compressibility divided by density of pure water ($\Delta\kappa_T/\rho^0$, solid curves, data from Figure 10a,b) by using the factors in (a) and experimental value for $\alpha^0/\rho^0 C_P^0$ in accordance with eq 10. The same adiabatic-isothermal shift was applied to the isothermal compressibility computed by pressure derivatives of fitted volume [lower pair of curves in (b), data for the lower solid curve in (b) are from Figure 10a] and to the isothermal compressibility determined using volume fluctuations [upper pair of curves in (b), data for upper solid curve in (b) are from Figure 10b].

These values are essentially equal to or at most 2.5 times the experimental partial molar adiabatic compressibility of a pair of independent alanine side chains which is estimated to be approximately 1.2×10^{-3} Å^3 atm^{-1} from measurements on Gly−X−Gly tripeptides.[166] Again, as in the above consideration of isothermal compressibility, the approximate numerical agreement between our simulated partial molar adiabatic compressibilities of two methanes and a corresponding experiment-based estimate lends credence to the two-methane compressibility effects predicted here.

IV. DISCUSSION: RAMIFICATIONS FOR PROTEIN FOLDING

In view of the biophysical significance of hydrophobic interactions,[8−10] insights into pressure-dependent protein folding can be gleaned from computational data on pressure-dependent pairwise hydrophobic interactions. Some progress has already been made in this direction by incorporating

dx.doi.org/10.1021/jp501935f | J. Phys. Chem. B 2014, 118, 7488−7509

pressure dependence of db height and ssm depth[38] in coarse-grained protein chain models.[178,179] Figure 13 provides a

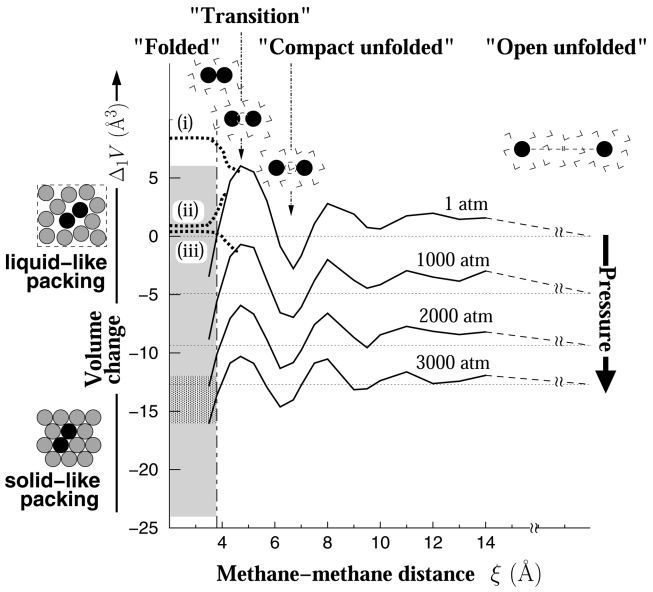

Figure 13. Conceptual links between two-methane volumetric properties and pressure-dependent protein folding behaviors. The vertical scale represents the relative volume $\Delta_1 V = \Delta_1 V(\xi,P)$ (in units of Å^3), which is defined as the volume of a pair of methanes ξ apart in water at a given pressure P minus the volume when the methanes are infinitely separated in water under P = 1 atm at T = 298.15 K. The $\Delta_1 V$ values for P = 1, 1000, 2000, and 3000 atm (solid curves) were obtained from the simulations described above (data from Figure 7). Each of the four horizontal dotted baselines marks the volume of a pair of infinitely separated methanes in water for the given pressure. Thus, although our simulations covered $\xi \leq 14$ Å, each volume curve should approach its baseline as $\xi \to \infty$ (this expected trend is indicated schematically by the broken dashed lines). Top: Water and methane molecules are depicted as in Figure 1. The drawings here illustrate that aqueous two-methane configurations near the db, ssm, and far-apart ($\xi \to \infty$) positions may serve as intuitive models, respectively, for elementary nonpolar interactions in the transition, compact unfolded, and open unfolded states of a protein, as the nonpolar residues are partially exposed to water in these states that are not well-packed. However, unlike the two-methane configuration at the cm position (vertical dotted-dashed lines) that are partially exposed to water, most of the nonpolar solutes in the folded state are not exposed to water. The shaded areas indicate approximate ranges of the partial molar volumes of two methanes in liquid-like or solid-like packing relative to the $\Delta_1 V$ baseline at P = 1 atm. (The two ranges overlap for ΔV_1 values spanning approximately between −12 and −16 Å^3). The thick dotted curves show hypothetical volume changes between the folded and transition states. The folded state can have a partial molar volume larger than that of typical liquid state [case (i)] if there is significant void volume in the protein core. Depending on the packing of the protein folded state and external pressure, the thick dotted curves show that the folded state can have a partial molar volume larger [(i) for P = 1 atm, (iii) for P = 1000 atm] or smaller [(ii) for P = 1 atm] than that of the folding/unfolding transition state.

panoramic view of most of our new simulation data together with physically plausible conceptual links between two-methane configurations and various protein conformational states. Volumes at different pressures are compared here on an equal footing in that all volumes are plotted relative to a common baseline. As suggested above, as a model system, a methane pair in water is more adequate for conformations with fully or partially exposed nonpolar groups than folded conformations with sequestered hydrophobics. Therefore, to address the energetic balance between the unfolded and folded states, rather than relying on the two-methane system alone, it is more appropriate to compare volumes of aqueous two-methane systems against pure-phase two-methane volumes with packing densities mimicking those in the sequestered cores of folded proteins. For this reason, the partial molar volumes of a pair of methanes under various liquid-like and solid-like packing conditions are featured in Figure 13 as well.

A. Volumes of Methane in Water versus Methane in Pure Liquid or Solid State. We utilize two experimental measurements of partial molar volume of methane to bracket a range of densities for liquid-like packing: $V_{\text{liquid}} \approx 63$ Å^3 for the liquid state at the boiling point of methane under P = 1 atm (T = 111.7 K),[180] and $V_{\text{liquid}} \approx 52$ Å^3 for the liquid state at the melting point of solid methane under P = 3186 atm (T = 156.97 K).[181] These values lead us to adopt an interval from 2 × 52 = 104 to 2 × 63 = 126 Å^3 as a reasonable range of excess volume for a pair of methanes under liquid-like packing. The corresponding $\Delta_1 V$ range is determined by using the experimental V_m at T = 298.15 K and P = 1 atm, which is 61.93 Å^3 (37.3 cm^3 mol^{-1})[120] and very close to our simulated value of 62.79 Å^3. Then, by using eq S7 in SI and the experimental κ_T^0 = 4.59 × 10^{-5} atm^{-1} (ref 147), the experimental excess volume of methane is ΔV = 60.1 ≈ 60 Å^3 and therefore the excess volume for a pair of methane is $2\Delta V \approx 120$ Å^3. Hence we arrive at a $\Delta_1 V$ range of [−16 Å^3, +6 Å^3] for liquid-like packing, that is, from 104−120 = −16 Å^3 to 126−120 = 6 Å^3 in Figure 13.

For solid-like packing, the single-methane partial molar volume of solid methane at the melting temperature T = 252.5 K under a high pressure of $P \approx 9692$ atm is $V_{\text{solid}} \approx 45$ Å^3 (derived from density data of Constantino and Daniels[182]). Because of the extremely high pressure under which this V_{solid} is measured, it may be viewed as an extremely low limit for solid-like methane partial molar volume. For the solid state along the methane melting curve under $P \lesssim 3000$ atm, a range of partial molar volumes from $V_{\text{solid}} \approx 50$ Å^3 to $V_{\text{solid}} \approx 54$ Å^3 was reported by Cheng et al. for pressures ranging from $P \sim 0.1$ atm to P = 3186 atm (melting temperature ranging from T = 90.69 to 156.97 K).[181] These values are consistent with estimates of 2.06 to 2.08 Å for the molecular radius R of methane from exerpimental crystallographic data or quantum mechanical calculations,[183] because the corresponding molecular volume $4\pi R^3/3$ divided by the face-centered cubic packing fraction $\pi/\sqrt{18}$ yields partial molar volumes from 49.5 Å^3 (for R = 2.06 Å) to 50.9 Å^3 (for R = 2.08 Å). From these considerations, we take 48−54 Å^3 as a reasonable range for solid-like single-methane excess volume. Accordingly, relative to the common baseline, the $\Delta_1 V$ values for solid-like packing in Figure 13 ranges from 2 × 48−120 = −24 Å^3 to 2 × 54−120 = −12 Å^3.

B. Two-Methane Contact Minimum May Not Be a Good Model for Folded States. In using two-methane simulations to address protein folding, the cm position, being the least water-exposed among aqueous two-methane configurations, is often taken as a model for conformations with properties similar to those of the folded state.[24,30,38] This approach has its utility. Nonetheless, because the methanes in the cm position are still significantly exposed to water, the physical correspondence between cm and folded state can be limited. More precisely, the adequacy of such a conceptual link depends on the issue being addressed. For instance, the heat

capacity of a protein generally decreases upon folding, but this trend is not universally reproduced by simulated cm properties. Although the heat capacity at cm relative to that at large ξ is negative for several water models,[26] it is notably not negative for TIP4P.[24−26] It remains to be ascertained whether this particular TIP4P prediction is artifactual; however, from a physical standpoint, it is clearly more appropriate to identify the partially water-exposed cm configuration with the nonpolar contacts in compact denatured states[31] rather than the contacts in the well-packed cores of folded proteins.

For this reason, instead of the cm, we consider the pure-phase liquid and solid states introduced above (Figure 13) as putative models for the folded state. Their packing densities showcase a physically viable range that might mimic those in the core of a folded protein. In applying these packing densities of pure methane under rather extreme pressure/temperature conditions (see above) to model folded-state packing densities under more moderate conditions studied here ($T \sim 300$ K, P = 1−3000 atm), we are stipulating that at least a subset of these packing densities is achievable in the folded protein core under more moderate conditions because the folded state is held together not only by van der Waals interactions among nonpolar groups (as in the pure methane phases) but also by covalent chain connectivity[124] and other types of intraprotein interactions such as hydrogen bonding, disulfide bonding, and salt bridges. Indeed, it has long been known that the compressibility of protein is solid-like[144] and that nonpolar solvents under ambient conditions are not good models for the interior of folded proteins because packing densities of nonpolar solvents are significantly lower than packing densities of protein cores.[118,119] By taking these experimental observations into consideration, our approach recognizes the contributions from the many types of specific interactions to the volumetric properties of protein folded states though we do not directly address these interactions in the present investigative framework.

C. Void Volume Is Critical in Determining Pressure Dependence. We now consider the implications of various putative folded-state packing densities in Figure 13. To explore possible folding scenarios, we contrast the volume of two methanes in a dense, water-free environment—which we assume to correspond to the interior of a folded protein—with that of two methanes in various aqueous configurations. As a model for real protein behaviors, it should be noted that our two-methane volumetric accounting is drastically simplified. For instance, in identifying the packing density of the folded state with that of the folded core, we are neglecting size- and curvature-sensitive contributions to pressure-dependent properties from the collective volumetric effects of nonpolar groups that remain partially exposed in the folded structure.[43] Nonetheless, as will be seen below, sufficient pertinent physics is captured by the present approach to provide conceptual advances and semiquantitative insights into pressure-dependent protein folding.

We first address equilibrium stability of the folded state relative to the unfolded state by comparing the Δ_1V volumes in Figure 13 for various putative folded states against the Δ_1V volumes for the large-ξ configurations (dotted horizontal baselines) corresponding to open unfolded states under different pressures. Figure 13 shows that if the core of protein is uniformly solid-like with minimal void volume situating within $\Delta_1V \lesssim -15$ Å^3 of the solid-like range (note that $\Delta_1V \lesssim -20$ Å^3 for a perfectly packed pure methane solid; see above), pressure denaturation would not be possible even at P = 3000 atm, because in that case, the volume of the model folded state has a smaller volume (lower Δ_1V) than not only the large-ξ model open unfolded state but also the lowest aqueous Δ_1V at ssm. This observation underscores the importance of considering a water-free pure phase rather than the aqueous cm configuration as a model for the folded state, because in this hypothetical situation, the picture deduced originally from analyzing aqueous PMFs alone that high pressure always induces water to penetrate the folded core[38] would not apply.

In this light, the experimental fact that many proteins do unfold under pressure[74] suggests that the packing densities of their folded cores at $P \approx 1$ atm should correspond to the middle or upper parts of the liquid-methane range in Figure 13 with $\Delta_1V \gtrsim 0$ [see examples provided by the thick dotted curves labeled (i) and (ii)]. In the context of our simple model, this means that the model folded state should have more void volumes than solid-state methane. This does not mean, however, that compressibility of the folded state is similar to that of nonpolar liquids. The reason, as emphasized above, is that in addition to van der Waals attractions between nonpolar groups, the folded protein is also held together by chain connectivity and other stabilizing forces. Indeed, even if we apply the highest compressibility in the $\sim 3-25 \times 10^{-6}$ atm^{-1} range for experimentally measured compressibilities of folded proteins[67,70,145,146] to a two-methane model folded state, the resulting $\partial\Delta_1V/\partial P \approx 3.0 \times 10^{-3}$ Å^3 atm^{-1} and thus the folded-state Δ_1V (on the left of Figure 13) would decrease by only ≈9 Å^3 over 3000 atm. This decrease is less than the ≈12.5 Å^3 decrease in Δ_1V for the large-ξ baseline (on the right of Figure 13) and the corresponding ≈12 Å^3 decrease in Δ_1V for the ssm position. Thus, in this picture, increase in pressure would lead to increasing destabilization of the folded state relative to both the open unfolded and compact unfolded states.

The consideration above thus highlights the central importance of voids, or "packing defects," in determining pressure-dependent protein behaviors, as has been elucidated by recent experimental advances.[86,184,185] A corollary of this principle, as discussed above, is that if a compact, folded-like polypeptide structure contains little void volume, it needs not unfold by pressure. This view is consistent with a recent experiment showing that the volume of a 21-amino-acid alanine-based peptide decreases, rather than increases, upon helix formation.[186] Interestingly, this observation also rationalizes the presence of residual helical structures in pressure-denatured proteins.[187] An earlier study by Chalikian and Macgregor also emphasizes the importance of folded-state packing density and void volumes in pressure denaturation. By computing Voronoi volumes of different constituent groups in folded proteins, they concluded that peptide groups are chiefly responsible, whereas nonpolar groups disfavor pressure denaturation of proteins.[84] This finding represents a significant conceptual advance. However, because packing of the protein core is a global process involving cooperative interactions among many constituent groups, the physical implications and predictive power of assigning specific intrinsic folded-state volumes to individual chemical groups remain to be delineated. Their picture of a pressure-denatured state, in contrast to that envisioned by the water penetration model,[38] is one in which the interior is "micelle-like" with the peptide groups more water-exposed than the nonpolar groups.[84] It would be extremely interesting to test this prediction experimentally as well as computationally in future studies.

dx.doi.org/10.1021/jp501935f | J. Phys. Chem. B 2014, 118, 7488−7509

D. Activation Volume and db: Transient and Permanent Voids. Shifting our attention from thermodynamics to kinetics, we now focus on the db-associated void volume which has been suggested to be a physical origin of activation volumes in protein folding.[99,100,105] Here, Figure 13 shows that a volume barrier is encountered in the transition region as the folded state (left) is approached from the unfolded states (right). This picture is consistent with experimental observations that activation volume of folding is almost always positive.[61,65,66,69,72,73,78−80] Our simulation results highlight a sterically driven increase in volume whenever two nonpolar groups come together in water, a process that is expected at the rate-limiting step of folding. Because of its geometric origin, this volume increase is a robust occurrence irrespective of the void volume entrapped by the final collapsed configurations of the nonpolar groups. In other words, we stipulate that although the *positive* void volume in the protein folded state can affect the sign of the activation volume of unfolding (see below), it is unlikely to affect the positive sign of the activation volume of folding because of an intrinsically *positive* contribution to the activation volume of folding from the hydrophobic collapse process. Nonetheless, activation volumes of folding in real proteins can be highly sensitive to mutations involving charged residues because of their effects on local water density. For instance, a single T62K substitution in staphylococcal nuclease (SNase) can reduce the substantial folding activation volume of the wildtype protein to zero.[82]

In the unfolding direction, the relationship between db-associated void volume and the activation volume of unfolding is more complex. If all of the void volume is transient in that the voids are essentially eliminated or significantly reduced when folding is completed (as envisioned in interpretative narratives of two-methane data that used the cm as model for the folded state), volume change would always be positive irrespective of whether one is going from the unfolded state or the folded state to the transition state. For example, in the study by Hummer et al.,[38] the computed volume changes from ssm to db and from cm to db are, respectively, $\Delta V^{\ddagger}(\text{ssm} \rightarrow \text{db}) \approx 3.8$ mL mol^{-1} and $\Delta V^{\ddagger}(\text{cm} \rightarrow \text{db}) \approx 1.6$ mL mol^{-1}. In the present simulation as well, the peak volume in Figure 8b is always larger than either the cm volume or first-minimum volume. However, because a significant void volume exists in the native structure, the volume change from the folded to the transition state is not necessarily positive. While recognizing that the folded state is dynamic and thus its void volume fluctuates, we refer to the voids in the folded state as "permanent" because its void volume is narrowly distributed (as reflected by its low compressibility), and thus, a well-defined average void volume likely persists for a much longer time scale than that of the transient voids in the transition state. During the folding process, as transient voids are eliminated when more and more of the folded state is formed, voids that are essentially permanent in the folded structure may develop concomitantly. Consequently, depending on the balance between transient and permanent void volumes and the packing density of the folded state, unfolding activation volume can be positive or negative. These two different scenarios are illustrated by the dotted curves in Figure 13 connecting the db $\Delta_1 V$ peak with hypothetical folded-state $\Delta_1 V$ volumes. Activation volume of unfolding is negative for a loosely packed folded state [dotted curve (i)] but it can be positive if the folded state is more densely packed [dotted curve (ii)]. Both possibilities have been observed experimentally: Whereas activation volume of unfolding of wildtype SNase at 25 °C and pH 6.0 is slightly negative and that of some SNase mutants can be much more negative,[79] activation volume of unfolding of the wildtype protein at 21 °C and pH 5.5 is positive.[61] Activation volume of the unfolding of cold-shock protein CspB at 25 °C and pH 7.0 is positive as well.[72] The SNase example indicates further that activation volume of unfolding is sensitive to external conditions. In a similar vein, Figure 13 illustrates a scenario in which the compressibility of the folded state is significantly smaller than that of the unfolded state [$\Delta_1 V$ of the folded state changes only slightly from (ii) to (iii) when P changes from 1 to 1000 atm]. In this hypothetical situation, the sign of activation volume of unfolding can change from positive under low pressures [dotted curve (ii)] to negative under higher pressures [dotted curve (iii)].

E. Volumetric and Enthalpic Barriers: Similarities and Differences. As mentioned above, desolvation of nonpolar solutes leads to transient voids because of geometric exclusion of water, also known as steric dewetting.[27,105] When similar sterics applies, transient voids and energetic barriers can also emerge in other contexts, such as between an amino nitrogen and a carbonyl oxygen that are close to each other but not hydrogen bonded.[186,188] Coarse-grained models indicate that db plays a central role in protein folding cooperativity.[94,100,141,189,190] A basic underlying principle is that db effectively restricts attractive intrachain interactions to a narrow spatial range[101] and that such narrowing has a general enhancing effect on the cooperativity of coil−globule transitions.[191]

In addition to contributing to volumetric barriers (i.e., activation volumes),[99,100,105] transient voids also lead to enthalpic barriers to protein folding.[27,100,105] Notably, experimentally observed enthalpic barriers to folding at room temperature are much larger than the small enthalpic barrier to three-methane association[27] and the slightly positive[41] or negative[24] barrier to two-methane association. In contrast, the enthalpic barrier in the simulated association of two α-helices is comparable to that in two-state-like protein folding. On the basis of these findings, it was argued that large fragments of a protein, similar in size to two helices, must come together at the rate-limiting step of two-state-like folding.[105] In view of the present two-methane data, a similar argument may be advanced for the activation volume of folding as well: Whereas the folding activation volume $\Delta V^{\ddagger}$ for wildtype SNase ≈55 mL mol^{-1} is comparable with the computed volume peak for the association of two polyalanine α-helices,[99,105] this $\Delta V^{\ddagger}$ is much larger than the $\Delta V \approx 6$ Å^3 (3.6 mL mol^{-1}) at the volume peak around db for two-methane association (Figure 8). Thus, as in the consideration of enthalpic barriers, this comparison of volumetric trends again suggests that large fragments of the protein come together simultaneously at the rate limiting step of folding.

Typically, at room temperature, the enthalpy of the folding/unfolding transition state is higher than both the folded and the unfolded states.[104,192] Thus, the enthalpy variation accompanying the folding process (unfolded → transition → folded) is nonmonotonic. Inasmuch as the decrease in enthalpy from the transition state to the folded state is partly accomplished by the elimination of transient voids in the transition state to enable tighter, energetically more favorable packing in the folded state, one expects this void-eliminating process to lead to a concomitant decrease in volume. However, because some of the permanent voids in the folded state may develop after the

dx.doi.org/10.1021/jp501935f | J. Phys. Chem. B 2014, 118, 7488−7509

transition state, the volume reduction due to the elimination of transient voids upon folding can be compensated to a degree, or even overcompensated, by the volume increase entailed by the development of permanent voids. Some permanent voids can also form at or prior to the transition state and thus contribute together with the transient voids to the activation volume of folding. As a result, whether the volume change along the protein folding pathway is monotonic or nonmonotonic can vary from protein to protein. It is noteworthy that volume variation along folding pathway has been used as a measure of the degree of dehydration relative to the folded state.[82] The above consideration, however, suggests that although such an interpretation of volume change can be applicable to permanent voids, it may not apply to transient voids. The reason is that the dewetted protein surfaces forming part of the boundary enveloping a transient void are already dehydrated. Thus, elimination of the transient void by tighter packing would not lead to an increase in solvation or decrease in dehydration.

Taken together, if the increase in permanent void overcompensates for the decrease in transient void during the protein's move from the transition to the folded state, the volumetric barrier to folding would resemble a plateau rather than a peak, resulting in a negative activation volume of unfolding [Figure 13, (i)] and a monotonic volume variation along the folding pathway. Alternatively, if the increase in permanent void compensates only partially for the decrease in transient void, the volumetric barrier to folding, like the enthalpic barrier, would take the form of a peak. In that case, the activation volume of unfolding is positive [Figure 13, (ii)]. In this regard, experimental observations of nonmontonic variation in volume along the folding pathway[61,72] is consistent with transient voids contributing to activation volume of folding. A basic difference remains, however, between the nonmontonic volume and enthalpy profiles: whereas folded-state volume is generally higher than that of the unfolded state,[61,72] the reverse is true for enthalpy at room temperature.[104,192]

F. Possible Nonzero Activation Compressibilities for Protein Folding and Unfolding. Our simulation shows that excess compressibility is highest near the db position (Figure 11), suggesting a positive contribution to activation compressibility from the transient voids in the protein folding transition state. Experimentally, activation compressibility in folding is manifested by the curvature in the plot of logarithmic folding and unfolding rates versus pressure. Such plots are often referred to as pressure chevrons. A pressure-chevron arm (for folding or unfolding) that concaves upward or downward indicates, respectively, a positive or negative activation compressibility. Early experiments by Suzuki on the pressure denaturation of ovalbumin and carbonylhemoglobin[53] suggest that the unfolding transition state of these proteins are significantly more compressible than their respective folded state, that is, the unfolding activation compressibility is positive, but those experiments did not address activation compresssibility in the folding direction. More recent experimental pressure chevron plots for other proteins,[79,80] however, exhibit largely linear folding and unfolding arms, indicating that activation compressibility is essentially zero for both folding and unfolding. One possible exception is the Y115W mutant of ribonuclease A under the condition of 50 °C+30% glycerol, for which the pressure-chevron folding arm (Figure 6 of ref 80) shows a small upward curvature consistent with a positive activation compressibility for folding. In the perspective expounded above, a lack of activation compressibility of folding suggests that the expected positive contribution to activation compressibility from transient voids is compensated by the concomitant development of less compressible, partially folded-like conformational structures (possibly with permanent voids) in the folding transition state.

G. Outlook and Concluding Remarks. It is clear from the above discussion that, as a physical probe, pressure perturbation has provided a wealth of information and insights into protein folding. In view of recent experimental advances[84,88,185−187,193] and growing theoretical interest in volumetric effects in peptide and proteins simulations[45,88,188] as well as in the study of elementary, model−compound interactions,[43,47,194−197] researchers are taking further advantage of the pressure variable to better understand protein conformational transitions.

By comparing the directly simulated distance-dependent volumes of a pair of methanes in water with volumes consistent with liquid- and solid-like packing, our work clarifies several key concepts in the relationship between volumetric effects in elementary hydrophobic interactions and those in protein folding. Although the detailed relationship between volumetric effects of small-molecule hydrophobic interactions and those of hydrophobic interactions at larger length scales remains to be delineated, the development of a void volume at the desolvation barrier is a robust geometric feature across different length scales.[103,105] Consistent with recent experiments,[84,88,185] our analysis points to the importance of void volumes in the folded states as a key determinant of how protein folding behaviors vary with pressure. Moreover, the transient void volumes in desolvation-barrier configurations associated with the enthalpic barriers to protein folding[100] are also seen as a likely contributor to the experimentally observed activation volumes of folding. However, because the approach toward the folded state often involves development of permanent voids, the physical picture can be complex. Different scenarios for the pressure dependence of equilibrium and kinetic properties of protein folding may apply to different proteins or the same protein under different conditions, hinging in large measure on the packing density of the folded state as well as the transient and permanent void volumes during the folding and unfolding processes.

While our simulation study has made quantitative and conceptual advances, the limited scope of the present work should be noted. Our focus here is on the effects of pressure on two-methane association as a model for hydrophobic interactions. As such, this work did not directly tackle other contributing driving forces in protein folding,[8−10] though covalent connectivity of the protein chain and involvement of forces other than hydrophobicity were invoked in the discussion of packing densities and compressibilities of folded structures. Nonetheless, it is worth mentioning that hydrogen bonds between backbone atoms, which could be energetically favorable to folding,[198] were not found to drive favorable interactions between peptides in previous explicit-water simulations,[103,199] suggesting that folded-state stabilization by hydrogen bonding is not entailed by the force fields used in these simulations.

At the two-methane level, one obvious extension of our work would be to study the combined effects of pressure and temperature, as has been pursued to some degree for single-methane solvation.[42] The present study touched upon temperature dependence but only very briefly. Indeed, as

dx.doi.org/10.1021/jp501935f | J. Phys. Chem. B 2014, 118, 7488−7509

noted above, the molecular basis of several peculiar features of the combined $P-T$ dependence of PMF in Figures 4 and 5 remain to be elucidated. Typically, proteins have an elliptic folding−unfolding phase diagram on the $P-T$ plane.[77,200] This behavior appears to follow from basic hydrophobic interactions, as suggested lately by an analytical theory[201] and a two-dimensional water model study.[132] These phase diagrams indicate that the folded state can have a smaller volume than the unfolded state at high temperatures, rather than the reverse under lower temperatures. Thermal expansivities of various protein conformational state have long been studied[70] but their physical origins are not yet well understood. A recent experiment on the ankyrin domain of the Notch receptor shows that the activation volume for unfolding turns from negative at low temperature to positive at higher temperature.[202] A more recent study relevant to the $P-T$ dependence of hydrophobic interactions involves experiments on hydrophobic homopolymer brushes showing that temperature and pressure have antagonistic effects on the conformational packing of the interfacial polymer chains: Whereas an increase in temperature leads to a more collapsed, well-packed state, an increase in pressure results in more open configurations. On balance, the pressure and temperature effects on the studied system compensate each other at an approximate rate of 100 atm/K.[203] Information from future studies of combined pressure−temperature dependence of hydrophobic interactions should provide useful physical insights to help decipher these intriguing experimental observations.

■ ASSOCIATED CONTENT

Supporting Information

Modeling and methodological details for the above-discussed results. This material is available free of charge via the Internet at http://pubs.acs.org.

■ AUTHOR INFORMATION

Corresponding Authors

*E-mail: cld@njit.edu.

*E-mail: chan@arrhenius.med.toronto.edu.

Notes

The authors declare no competing financial interest.

■ ACKNOWLEDGMENTS

We thank Tigran Chalikian, Alfons Geiger, Cathy Royer, Jerson Silva, and Roland Winter for very helpful discussions, and we thank Allison Ferguson, Maria Sabaye Moghaddam, Seishi Shimizu, and Nicolas Taulier for technical help during the early stages of this investigation. H.S.C. is particularly grateful to Cathy Royer and Roland Winter for the opportunities to present the ideas and results in this work to their research groups and colleagues and for their subsequent insightful comments and suggestions. This work was supported by research grants from the Canadian Institutes of Health Research and the Canada Research Chairs Program to H.S.C. We are also grateful to SHARCNET and SciNet of Compute Canada for their generous allotments of computational resources.

■ REFERENCES

(1) Brandts, J. F. Conformational Transitions of Proteins in Water and in Aqueous Mixtures. In *Structure and Stability of Biological Macromolecules*; Timasheff, S. N., Fasman, G. D., Eds.; Marcel Dekker, Inc.: New York, 1969; pp 213−290.

(2) Levy, Y.; Onuchic, J. N. Water Mediation in Protein Folding and Molecular Recognition. *Annu. Rev. Biophys. Biomol. Struct.* **2006**, *35*, 389−415.

(3) Ball, P. Water as An Active Constituent in Cell Biology. *Chem. Rev.* **2008**, *108*, 74−108.

(4) Kauzmann, W. Some Factors in the Interpretation of Protein Denaturation. *Adv. Protein Chem.* **1959**, *14*, 1−63.

(5) Tanford, C. Protein Denaturation. *Adv. Protein Chem.* **1968**, *23*, 121−281.

(6) Lumry, R.; Biltonen, R. Thermodynamic and Kinetic Aspects of Protein Conformations in Relation to Physiological Function. In *Structure and Stability of Biological Macromolecules*; Timasheff, S. N., Fasman, G. D., Eds.; Marcel Dekker, Inc.: New York, 1969; pp 65−212.

(7) Baldwin, R. L. Temperature Dependence of the Hydrophobic Interaction in Protein Folding. *Proc. Natl. Acad. Sci. U.S.A.* **1986**, *83*, 8069−8072.

(8) Dill, K. A. Dominant Forces in Protein Folding. *Biochemistry* **1990**, *29*, 7133−7155.

(9) Yang, A.-S.; Honig, B. Free Energy Balance in Protein Folding. *Adv. Protein Chem.* **1995**, *46*, 27−58.

(10) Pace, C. N.; Shirley, B. A.; McNutt, M.; Gajiwala, K. Forces Contributing to the Conformational Stability of Proteins. *FASEB J.* **1996**, *10*, 75−83.

(11) Chan, H. S. Modeling Protein Density of States: Additive Hydrophobic Effects are Insufficient for Calorimetric Two-State Cooperativity. *Proteins* **2000**, *40*, 543−571.

(12) Blokzijl, W.; Engberts, J. B. F. N. Hydrophobic Effects − Opinions and Facts. *Angew. Chem., Int. Ed. Engl.* **1993**, *32*, 1545−1579.

(13) Lazaridis, T. Solvent Size vs Cohesive Energy as the Origin of Hydrophobicity. *Acc. Chem. Res.* **2001**, *34*, 931−937.

(14) Southall, N. T.; Dill, K. A.; Haymet, A. D. J. A View of the Hydrophobic Effect. *J. Phys. Chem. B* **2002**, *106*, 521−533.

(15) Berne, B. J.; Weeks, J. D.; Zhou, R. Dewetting and Hydrophobic Interaction in Physical and Biological Systems. *Annu. Rev. Phys. Chem.* **2009**, *60*, 85−103.

(16) Baldwin, R. L. The New View of Hydrophobic Free Energy. *FEBS Lett.* **2013**, *587*, 1062−1066.

(17) Murphy, K. P.; Gill, S. J. Solid Model Compounds and the Thermodynamics of Protein Unfolding. *J. Mol. Biol.* **1991**, *222*, 699−709.

(18) Myers, J. K.; Pace, C. N.; Scholtz, J. M. Denaturant *m*-values and Heat Capacity Changes: Relation to Changes in Accessible Surface Areas of Protein Unfolding. *Protein Sci.* **1995**, *4*, 2138−2148.

(19) Makhatadze, G. I.; Privalov, P. L. Energetics of Protein Structure. *Adv. Protein Chem.* **1995**, *47*, 307−425.

(20) Robertson, A. D.; Murphy, K. P. Protein Structure and the Energetics of Protein Stability. *Chem. Rev.* **1997**, *97*, 1251−1267.

(21) Chalikian, T. V. Volumetric Properties of Proteins. *Annu. Rev. Biophys. Biomol. Struct.* **2003**, *32*, 207−235.

(22) Auton, A.; Bolen, D. W. Predicting the Energetics of Osmolyte-Induced Protein Folding/Unfolding. *Proc. Natl. Acad. Sci. U.S.A.* **2005**, *102*, 15065−15068.

(23) Lüdemann, S.; Abseher, R.; Schreiber, H.; Steinhauser, O. The Temperature Dependence of Hydrophobic Association in Water. Pair Versus Bulk Hydrophobic Interactions. *J. Am. Chem. Soc.* **1997**, *119*, 4206−4213.

(24) Shimizu, S.; Chan, H. S. Temperature Dependence of Hydrophobic Interactions: A Mean Force Perspective, Effects of Water Density, and Non-Additivity of Thermodynamic Signatures. *J. Chem. Phys.* **2000**, *113*, 4683−4700.

(25) Shimizu, S.; Chan, H. S. Configuration-Dependent Heat Capacity of Pairwise Hydrophobic Interactions. *J. Am. Chem. Soc.* **2001**, *123*, 2083−2084.

(26) Paschek, D. Temperature Dependence of the Hydrophobic Hydration and Interaction of Simple Solutes: An Examination of Five Popular Water Models. *J. Chem. Phys.* **2004**, *120*, 6674−6690.

(27) Moghaddam, M. S.; Shimizu, S.; Chan, H. S. Temperature Dependence of Three-Body Hydrophobic Interactions: Potential of

Mean Force, Enthalpy, Entropy, Heat Capacity, and Nonadditivity. *J. Am. Chem. Soc.* **2005**, *127*, 303−316.
(28) Ghosh, T.; García, A. E.; Garde, S. Water-Mediated Three-Particle Interactions Between Hydrophobic Solutes: Size, Pressure, and Salt Effects. *J. Phys. Chem. B* **2003**, *107*, 612−617.
(29) Thomas, A. S.; Elcock, A. H. Molecular Dynamics Simulations of Hydrophobic Associations in Aqueous Salt Solutions Indicate a Connection Between Water Hydrogen Bonding and the Hofmeister Effect. *J. Am. Chem. Soc.* **2007**, *129*, 14887−14898.
(30) Wallqvist, A.; Covell, D. G.; Thirumalai, D. Hydrophobic Interactions in Aqueous Urea Solutions with Implications for the Mechanism of Protein Denaturation. *J. Am. Chem. Soc.* **1998**, *120*, 427−428.
(31) Shimizu, S.; Chan, H. S. Origins of Protein Denatured State Compactness and Hydrophobic Clustering in Aqueous Urea: Inferences from Nonpolar Potentials of Mean Force. *Proteins* **2002**, *49*, 560−566.
(32) Graziano, G. Size and Temperature Dependence of Hydrocarbon Solubility in Concentrated Aqueous Solutions of Urea and Guanidine Hydrochloride. *Can. J. Chem.* **2002**, *80*, 388−400.
(33) O'Brien, E. P.; Dima, R. I.; Brooks, B.; Thirumalai, D. Interactions Between Hydrophobic and Ionic Solutes in Aqueous Guanidinium Chloride and Urea Solutions: Lessons for Protein Denaturation Mechanism. *J. Am. Chem. Soc.* **2007**, *129*, 7346−7353.
(34) Athawale, M. V.; Sarupria, S.; Garde, S. Enthalpy-Entropy Contributions to Salt and Osmolyte Effects on Molecular-Scale Hydrophobic Hydration and Interactions. *J. Phys. Chem. B* **2008**, *112*, 5661−5670.
(35) Wallqvist, A. Pressure Dependence of Methane Solvation in Aqueous Mixtures and the Relation to the Structure of Liquid Water. *J. Chem. Phys.* **1992**, *96*, 1655−1656.
(36) Matubayasi, N.; Levy, R. M. Thermodynamics of the Hydration Shell. 2. Excess Volume and Compressibility of a Hydrophobic Solute. *J. Phys. Chem.* **1996**, *100*, 2681−2688.
(37) Payne, V. A.; Matubayasi, N.; Murphy, L. R.; Levy, R. M. Monte Carlo Study of the Effect of Pressure on Hydrophobic Association. *J. Phys. Chem. B* **1997**, *101*, 2054−2060.
(38) Hummer, G.; Garde, S.; García, A. E.; Paulaitis, M. E.; Pratt, L. R. The Pressure Dependence of Hydrophobic Interactions is Consistent with the Observed Pressure Denaturation of Proteins. *Proc. Natl. Acad. Sci. U.S.A.* **1998**, *95*, 1552−1555.
(39) Chau, P.-L.; Mancera, R. L. Computer Simulation of the Structural Effect of Pressure on the Hydrophobic Hydration of Methane. *Mol. Phys.* **1999**, *96*, 109−122.
(40) Ghosh, T.; García, A. E.; Garde, S. Molecular Dynamics Simulations of Pressure Effects on Hydrophobic Interactions. *J. Am. Chem. Soc.* **2001**, *123*, 10997−11003.
(41) Ghosh, T.; García, A. E.; Garde, S. Enthalpy and Entropy Contributions to the Pressure Dependence of Hydrophobic Interactions. *J. Chem. Phys.* **2002**, *116*, 2480−2486.
(42) Moghaddam, M. S.; Chan, H. S. Pressure and Temperature Dependence of Hydrophobic Hydration: Volumetric, Compressibility, and Thermodynamic Signatures. *J. Chem. Phys.* **2007**, *126*, 114507.
(43) Sarupria, S.; Garde, S. Quantifying Water Density Fluctuations and Compressibility of Hydration Shells of Hydrophobic Solutes and Proteins. *Phys. Rev. Lett.* **2009**, *103*, 037803.
(44) Floris, F. M. Nonideal Effects on the Excess Volume from Small to Large Cavities in TIP4P Water. *J. Phys. Chem. B* **2004**, *41*, 16244−16249.
(45) Sarupria, S.; Ghosh, T.; García, A. E.; Garde, S. Studying Pressure Denaturation of a Protein by Molecular Dynamics Simulations. *Proteins* **2010**, *78*, 1641−1651.
(46) Patel, N.; Dubins, D. N.; Pomès, R.; Chalikian, T. V. Parsing Partial Molar Volumes of Small Molecules: A Molecular Dynamics Study. *J. Phys. Chem. B* **2011**, *115*, 4856−4862.
(47) Voloshin, V. P.; Medvedev, N. N.; Andrews, M. N.; Burri, R. R.; Winter, R.; Geiger, A. Volumetric Properties of Hydrated Peptides: Voronoi-Delaunay Analysis of Molecular Simulation Runs. *J. Phys. Chem. B* **2011**, *115*, 14217−14228.
(48) Patel, N.; Dubins, D. N.; Pomès, R.; Chalikian, T. V. Size Dependence of Cavity Volume: A Molecular Dynamics Study. *Biophys. Chem.* **2012**, *161*, 46−49.
(49) Spooner, J.; Wiebe, H.; Boon, N.; Deglint, E.; Edwards, E.; Yanciw, B.; Patton, B.; Thiele, L.; Dance, P.; Weinberg, N. Molecular Dynamics Calculation of Molecular Volumes and Volumes of Activation. *Phys. Chem. Chem. Phys.* **2012**, *14*, 2264−2277.
(50) Pratt, L. R.; Chandler, D. Theory of Hydrophobic Effect. *J. Chem. Phys.* **1977**, *67*, 3683−3704.
(51) Bridgman, P. W. The Coagulation of Albumen by Pressure. *J. Biol. Chem.* **1914**, *19*, 511−513.
(52) Curl, A. L.; Jansen, E. F. Effect of High Pressures on Trypsin and Chymotrypsin. *J. Biol. Chem.* **1950**, *184*, 45−54.
(53) Suzuki, K. Studies on the Kinetics of Protein Denaturation under High Pressure. *Rev. Phys. Chem. Japan* **1960**, *29*, 91−98.
(54) Suzuki, K.; Suzuki, C.; Miyosawa, Y. Protein Denaturation by High Pressure: Measurements of Turbidity of Isoelectric Ovalbumin and Horse Serum Albumin Under High Pressure. *Arch. Biochem. Biophys.* **1963**, *101*, 225−228.
(55) Brandts, J. F.; Oliveira, R. J.; Westort, C. Thermodynamics of Protein Denaturation: Effect of Pressure on Denaturation of Ribonuclease A. *Biochemistry* **1970**, *9*, 1038−1047.
(56) Hawley, S. A. Reversible Pressure-Temperature Denaturation of Chymotrypsinogen. *Biochemistry* **1971**, *10*, 2436−2442.
(57) Zipp, A.; Kauzmann, W. Pressure Denaturation of Metmyoglobin. *Biochemistry* **1973**, *12*, 4217−4228.
(58) Silva, J. L.; Weber, G. Pressure Stability of Proteins. *Annu. Rev. Phys. Chem.* **1993**, *44*, 89−113.
(59) Gross, M.; Jaenicke, R. Protein Under Pressure: The Influence of High Hydrostatic Pressure on Structure, Function and Assembly of Proteins and Protein Complexes. *Eur. J. Biochem.* **1994**, *221*, 617−630.
(60) Hinz, H.-J.; Vogl, T.; Meyer, R. An Alternative Interpretation of the Heat Capacity Changes Associated with Protein Unfolding. *Biophys. Chem.* **1994**, *52*, 275−285; Erratum: **1995**, *53*, 291.
(61) Vidugiris, G. J. A.; Markley, J. L.; Royer, C. A. Evidence for a Molten Globule-Like Transition State in Protein Folding From Determination of Activation Volumes. *Biochemistry* **1995**, *34*, 4909−4912.
(62) Zhang, J.; Peng, X.; Jonas, A.; Jonas, J. NMR Study of the Cold, Heat, and Pressure Unfolding of Ribonuclease A. *Biochemistry* **1995**, *34*, 8631−8641.
(63) Mozhaev, V. V.; Heremans, K.; Frank, J.; Masson, P.; Balny, C. High Pressure Effects on Protein Structure and Function. *Proteins* **1996**, *24*, 81−91.
(64) Prehoda, K. E.; Mooberry, E. S.; Markley, J. L. Pressure Denaturation of Proteins: Evaluation of Compressibility Effects. *Biochemistry* **1998**, *37*, 5785−5790.
(65) Desai, G.; Panick, G.; Zein, M.; Winter, R.; Royer, C. A. Pressure-Jump Studies of the Folding/Unfolding of *Trp* Repressor. *J. Mol. Biol.* **1999**, *288*, 461−475.
(66) Mohana-Borges, R.; Silva, J. L.; Ruiz-Sanz, J.; de Prat-Gay, G. Folding of a Pressure-Denatured Model Protein. *Proc. Natl. Acad. Sci. U.S.A.* **1999**, *96*, 7888−7893.
(67) Filfil, R.; Chalikian, T. V. Volumetric and Spectroscopic Characterizations of the Native and Acid-Induced Denatured States of Staphylococcal Nuclease. *J. Mol. Biol.* **2000**, *299*, 827−842.
(68) Lassalle, M. W.; Yamada, H.; Akasaka, K. The Pressure-Temperature Free Energy Landscape of Staphylococcal Nuclease Monitored by H-1 NMR. *J. Mol. Biol.* **2000**, *298*, 293−302.
(69) Pappenberger, G.; Saudan, C.; Becker, M.; Merbach, A. E.; Kiefhaber, T. Denaturant-Induced Movement of the Transition State of Protein Folding Revealed by High-Pressure Stopped-Flow Measurements. *Proc. Natl. Acad. Sci. U.S.A.* **2000**, *97*, 17−22.
(70) Seemann, H.; Winter, R.; Royer, C. A. Volume, Expansivity and Isothermal Compressibility Changes Associated with Temperature and Pressure Unfolding of Staphylococcal Nuclease. *J. Mol. Biol.* **2001**, *307*, 1091−1102.

(71) Gekko, K. Compressibility Gives New Insight Into Protein Dynamics and Enzyme Function. *Biochim. Biophys. Acta* **2002**, *1595*, 382−386.
(72) Jacob, M. H.; Saudan, C.; Holtermann, G.; Martin, A.; Perl, D.; Merbach, A. E.; Schmid, F. X. Water Contributes Actively to the Rapid Crossing of a Protein Unfolding Barrier. *J. Mol. Biol.* **2002**, *318*, 837−845.
(73) Kitahara, R.; Royer, C.; Yamada, H.; Boyer, M.; Saldana, J. L.; Akasaka, K.; Roumestand, C. Equilibrium and Pressure-Jump Relaxation Studies of the Conformational Transitions of $P13^{MTCP1}$. *J. Mol. Biol.* **2002**, *320*, 609−628.
(74) Royer, C. A. Revisiting Volume Changes in Pressure-Induced Protein Unfolding. *Biochim. Biophys. Acta* **2002**, *1595*, 201−209.
(75) Smeller, L. Pressure-Temperature Phase Diagrams of Biomolecules. *Biochim. Biophys. Acta* **2002**, *1595*, 11−29.
(76) Taulier, N.; Chalikian, T. V. Compressibility of Protein Transitions. *Biochim. Biophys. Acta* **2002**, *1595*, 48−70.
(77) Ravindra, R.; Winter, R. On the Temperature-Pressure Free-Energy Landscape of Proteins. *ChemPhysChem* **2003**, *4*, 359−365.
(78) Tan, C.-Y.; Xu, C.-H.; Wong, J.; Shen, J.-R.; Sakuma, S.; Yamamoto, Y.; Lange, R.; Balny, C.; Ruan, K.-C. Pressure Equilibrium and Jump Study on Unfolding of 23-kDa Protein from Spinach Photosystem II. *Biophys. J.* **2005**, *88*, 1264−1275.
(79) Brun, L.; Isom, D. G.; Velu, P.; Garcia-Moreno, B.; Royer, C. A. Hydration of the Folding Transition State Ensemble of a Protein. *Biochemistry* **2006**, *45*, 3473−3480.
(80) Font, J.; Torrent, J.; Ribo, M.; Laurents, D. V.; Balny, C.; Vilanova, M.; Lange, R. Pressure-Jump-Induced Kinetics Reveals a Hydration Dependent Folding/Unfolding Mechanism of Ribonuclease A. *Biophys. J.* **2006**, *91*, 2264−2274.
(81) Meersman, F.; Dobson, C. M.; Heremans, K. Protein Unfolding, Amyloid Fibril Formation and Configurational Energy Landscapes under High Pressure Conditions. *Chem. Soc. Rev.* **2006**, *35*, 908−917.
(82) Mitra, L.; Hata, K.; Kono, R.; Maeno, A.; Isom, D.; Rouget, J. B.; Winter, R.; Akasaka, K.; Garcia-Moreno, B.; Royer, C. A. V_i-Value Analysis: A Pressure-Based Method for Mapping the Folding Transition State Ensemble of Proteins. *J. Am. Chem. Soc.* **2007**, *129*, 14108−14109.
(83) Winter, R.; Lopes, D.; Grudzielanek, S.; Vogtt, K. Towards an Understanding of the Temperature/Pressure Configurational and Free-Energy Landscape of Biomolecules. *J. Non-Equilib. Thermodyn.* **2007**, *32*, 41−97.
(84) Chalikian, T. V.; Macgregor, R. B., Jr. Origins of Pressure-Induced Protein Transitions. *J. Mol. Biol.* **2009**, *394*, 834−842.
(85) Schroer, M. A.; Paulus, M.; Jeworrek, C.; Krywka, C.; Schmacke, S.; Zhai, Y.; Wieland, D. C. F.; Sahle, C. J.; Chimenti, M.; Royer, C. A.; Garcia-Moreno, B.; Tolan, M.; Winter, R. High-Pressure SAXS Study of Folded and Unfolded Ensembles of Proteins. *Biophys. J.* **2010**, *99*, 3430−3437.
(86) Rouget, J.-B.; Aksel, T.; Roche, J.; Saldana, J.-L.; García, A. E.; Barrick, D.; Royer, C. A. Size and Sequence and the Volume Change of Protein Folding. *J. Am. Chem. Soc.* **2011**, *133*, 6020−6027.
(87) Royer, C.; Winter, R. Protein Hydration and Volumetric Properties. *Curr. Opin. Colloid Interface Sci.* **2011**, *16*, 568−571.
(88) Roche, J.; Caro, J. A.; Norberto, D. R.; Barthe, P.; Roumestand, C.; Schlessman, J. L.; García, A. E.; García-Moreno, B.; Royer, C. A. Cavities Determine the Pressure Unfolding of Proteins. *Proc. Natl. Acad. Sci. U.S.A.* **2012**, *109*, 6945−6950.
(89) Wood, R. H.; Thompson, P. T. Differences Between Pair and Bulk Hydrophobic Interactions. *Proc. Natl. Acad. Sci. U.S.A.* **1990**, *87*, 8921−8927.
(90) Shortle, D.; Ackerman, M. S. Persistence of Native-Like Topology in a Denatured Protein in 8 M Urea. *Science* **2001**, *293*, 487−489.
(91) Klein-Seetharaman, J.; Oikawa, M.; Grimshaw, S. B.; Wirmer, J.; Duchardt, E.; Ueda, T.; Imoto, T.; Smith, L. J.; Dobson, C. M.; Schwalbe, H. Long-Range Interactions Within a Nonnative Protein. *Science* **2002**, *295*, 1719−1722.
(92) Rank, J. A.; Baker, D. A Desolvation Barrier to Hydrophobic Cluster Formation May Contribute to the Rate-Limiting Step in Protein Folding. *Protein Sci.* **1997**, *6*, 347−354.
(93) Sheinerman, F. B.; Brooks, C. L. Calculations on Folding of Segment B1 of Streptococcal Protein G. *J. Mol. Biol.* **1998**, *278*, 439−456.
(94) Cheung, M. S.; García, A. E.; Onuchic, J. N. Protein Folding Mediated by Solvation: Water Expulsion and Formation of the Hydrophobic Core Occur after the Structural Collapse. *Proc. Natl. Acad. Sci. U.S.A.* **2002**, *99*, 685−690.
(95) Liu, Z.; Chan, H. S. Desolvation is a Likely Origin of Robust Enthalpic Barriers to Protein Folding. *J. Mol. Biol.* **2005**, *349*, 872−889.
(96) Zhang, Z.; Chan, H. S. Transition Paths, Diffusive Processes, and Preequilibria of Protein Folding. *Proc. Natl. Acad. Sci. U.S.A.* **2012**, *109*, 20919−20924.
(97) Plaxco, K. W.; Simons, K. T.; Baker, D. Contact Order, Transition State Placement and the Refolding Rates of Single Domain Proteins. *J. Mol. Biol.* **1998**, *277*, 985−994.
(98) Chan, H. S. Protein Folding: Matching Speed and Locality. *Nature* **1998**, *392*, 761−763.
(99) Ferguson, A.; Liu, Z.; Chan, H. S. Desolvation Barrier Effects are a Likely Contributor to the Remarkable Diversity in the Folding Rates of Small Proteins. *J. Mol. Biol.* **2009**, *389*, 619−636; Corrigendum: **2010**, *401*, 153.
(100) Chan, H. S.; Zhang, Z.; Wallin, S.; Liu, Z. Cooperativity, Local-Nonlocal Coupling, and Nonnative Interactions: Principles of Protein Folding from Coarse-Grained Models. *Annu. Rev. Phys. Chem.* **2011**, *62*, 301−326.
(101) Kaya, H.; Uzunoğlu, Z.; Chan, H. S. Spatial Ranges of Driving Forces are a Key Determinant of Protein Folding Cooperativity and Rate Diversity. *Phys. Rev. E* **2013**, *88*, 044701.
(102) Dias, C. L.; Karttunen, M.; Chan, H. S. Hydrophobic Interactions in the Formation of Secondary Structures in Small Peptides. *Phys. Rev. E* **2011**, *84*, 041931.
(103) Narayanan, C.; Dias, C. L. Hydrophobic Interactions and Hydrogen Bonds in β-Sheet Formation. *J. Chem. Phys.* **2013**, *139*, 115103.
(104) Jackson, S. E.; Fersht, A. R. Folding of Chymotrypsin Inhibitor 2. 2. Influence of Proline Isomerization on the Folding Kinetics and Thermodynamic Characterization of the Transition State of Folding. *Biochemistry* **1991**, *30*, 10436−10443.
(105) MacCallum, J. L.; Moghaddam, M. S.; Chan, H. S.; Tieleman, D. P. Hydrophobic Association of α-Helices, Steric Dewetting and Enthalpic Barriers to Protein Folding. *Proc. Natl. Acad. Sci. U.S.A.* **2007**, *104*, 6206−6210.
(106) Choudhury, N.; Pettitt, B. M. Enthalpy-Entropy Contributions to the Potential of Mean Force of Nanoscopic Hydrophobic Solutes. *J. Phys. Chem. B* **2006**, *110*, 8459−8463.
(107) Nishii, I.; Kataoka, M.; Tokunaga, F.; Goto, Y. Cold Denaturation of the Molten Globule States of Apomyoglobin and a Profile for Protein Folding. *Biochemistry* **1994**, *33*, 4903−4909.
(108) Lum, K.; Chandler, D.; Weeks, J. D. Hydrophobicity at Small and Large Length Scales. *J. Phys. Chem. B* **1999**, *103*, 4570−4577.
(109) Zhou, R.; Huang, X.; Margulis, C. J.; Berne, B. J. Hydrophobic Collapse in Multidomain Protein Folding. *Science* **2004**, *305*, 1605−1609.
(110) Choudhury, N.; Pettitt, B. M. On the Mechanism of Hydrophobic Association of Nanoscopic Solutes. *J. Am. Chem. Soc.* **2005**, *127*, 3556−3567.
(111) Choudhury, N.; Pettitt, B. M. The Dewetting Transition and the Hydrophobic Effect. *J. Am. Chem. Soc.* **2007**, *129*, 4847−4852.
(112) Kaya, H.; Chan, H. S. Contact Order Dependent Protein Folding Rates: Kinetic Consequences of a Cooperative Interplay Between Favorable Nonlocal Interactions and Local Conformational Preferences. *Proteins* **2003**, *52*, 524−533.
(113) Chen, T.; Chan, H. S. Effects of Desolvation Barriers and Sidechains on Local-Nonlocal Coupling and Chevron Behaviors in

Coarse-Grained Models of Protein Folding. *Phys. Chem. Chem. Phys.* **2014**, *16*, 6460−6479.
(114) Kallmeyer, J.; Pockalny, R.; Adhikari, R. R.; Smith, D. C.; D'Hondt, S. Global Distribution of Microbial Abundance and Biomass in Subseafloor Sediment. *Proc. Natl. Acad. Sci. U.S.A.* **2012**, *109*, 16213−16216.
(115) Daniel, I.; Oger, P.; Winter, R. Origins of Life and Biochemistry Under High-Pressure Conditions. *Chem. Soc. Rev.* **2006**, *35*, 858−875.
(116) Wu, H. Studies on Denaturation of Proteins. 13. A Theory of Denaturation. *Chin. J. Physiol.* **1931**, *5*, 321−344; Reprinted in *Adv. Protein Chem.* **1995**, *46*, 6−26.
(117) Edsall, J. T. Wu Hsien and the First Theory of Protein Denaturation (1931). *Adv. Protein Chem.* **1995**, *46*, 1−5.
(118) Chalikian, T. V.; Breslauer, K. J. On Volume Changes Accompanying Conformational Transitions of Biopolymers. *Biopolymers* **1996**, *39*, 619−626.
(119) Kauzmann, W. Protein Stabilization: Thermodynamics of Unfolding. *Nature* **1987**, *325*, 763−764.
(120) Masterton, W. L. Partial Molar Volumes of Hydrocarbons in Water Solution. *J. Chem. Phys.* **1954**, *22*, 1830−1833.
(121) Friedman, M. E.; Scheraga, H. A. Volume Changes in Hydrocarbon-Water Systems. Partial Molal Volumes of Alcohol−Water Solutions. *J. Phys. Chem.* **1965**, *69*, 3795−3800.
(122) Sawamura, S.; Kitamura, K.; Taniguchi, Y. Effect of Pressure on the Solubilities of Benzene and Alkylbenzenes in Water. *J. Phys. Chem.* **1989**, *93*, 4931−4935.
(123) Schellman, J. A. The Stability of Hydrogen-Bonded Peptide Structures in Aqueous Solution. *C. R. Trav. Lab. Carlsberg, Ser. Chim.* **1955**, *29*, 230−259.
(124) Hvidt, A. Discussion of Pressure-Volume Effects in Aqueous Protein Solutions. *J. Theor. Biol.* **1975**, *50*, 245−252.
(125) García, A. E.; Hummer, G. Water Penetration and Escape in Proteins. *Proteins* **2000**, *38*, 261−272.
(126) Imai, T.; Ohyama, S.; Kovalenko, A.; Hirata, F. Theoretical Study of the Partial Molar Volume Change Associated with the Pressure-Induced Structural Transition of Ubiquitin. *Protein Sci.* **2007**, *16*, 1927−1933.
(127) Vajpai, N.; Nisius, L.; Wiktor, M.; Grzesiek, S. High-Pressure NMR Reveals Close Similarity between Cold and Alcohol Protein Denaturation in Ubiquitin. *Proc. Natl. Acad. Sci. U.S.A.* **2013**, *110*, E368−E376.
(128) Panick, G.; Malessa, R.; Winter, R.; Rapp, G.; Frye, K. J.; Royer, C. A. Structural Characterization of the Pressure-Denatured State and Unfolding/Refolding Kinetics of Staphylococcal Nuclease by Synchrotron Small-Angle X-ray Scattering and Fourier-Transform Infrared Spectroscopy. *J. Mol. Biol.* **1998**, *275*, 389−402.
(129) Woenckhaus, J.; Kohling, R.; Thiyagarajan, P.; Littrell, K. C.; Seifert, S.; Royer, C. A.; Winter, R. Pressure-Jump Small-Angle X-ray Scattering Detected Kinetics of Staphylococcal Nuclease Folding. *Biophys. J.* **2001**, *80*, 1518−1523.
(130) Paliwal, A.; Asthagiri, D.; Bossev, D. P.; Paulaitis, M. E. Pressure Denaturation of Staphylococcal Nuclease Studied by Neutron Small-Angle Scattering and Molecular Simulation. *Biophys. J.* **2004**, *87*, 3479−3492.
(131) Paschek, D.; Nonn, S.; Geiger, A. Low-Temperature and High-Pressure Induced Swelling of a Hydrophobic Polymer-Chain in Aqueous Solution. *Phys. Chem. Chem. Phys.* **2005**, *7*, 2780−2786.
(132) Dias, C. L. Unifying Microscopic Mechanism for Pressure and Cold Denaturations of Proteins. *Phys. Rev. Lett.* **2012**, *109*, 048104.
(133) Dill, K. A.; Alonso, D. O. V.; Hutchinson, K. Thermal Stabilities of Globular Proteins. *Biochemistry* **1989**, *28*, 5439−5449.
(134) Dias, C. L.; Ala-Nissila, T.; Karttunen, M.; Vattulainen, I.; Grant, M. Microscopic Mechanism for Cold Denaturation. *Phys. Rev. Lett.* **2008**, *100*, 118101.
(135) Dias, C. L.; Ala-Nissila, T.; Wong-ekkabut, J.; Vattulainen, I.; Grant, M.; Karttunen, M. The Hydrophobic Effect and its Role in Cold Denaturation. *Cryobiology* **2010**, *60*, 91−99.
(136) Silverstein, K. A. T.; Haymet, A. D. J.; Dill, K. A. A Simple Model of Water and the Hydrophobic Effect. *J. Am. Chem. Soc.* **1998**, *120*, 3166−3175.
(137) Scalley, M. L.; Baker, D. Protein Folding Kinetics Exhibit an Arrhenius Temperature Dependence when Corrected for the Temperature Dependence of Protein Stability. *Proc. Natl. Acad. Sci. U.S.A.* **1997**, *94*, 10636−10640.
(138) Kuhlman, B.; Luisi, D. L.; Evans, P. A.; Raleigh, D. P. Global Analysis of the Effects of Temperature and Denaturant on the Folding and Unfolding Kinetics of the N-Terminal Domain of the Protein L9. *J. Mol. Biol.* **1998**, *284*, 1661−1670.
(139) Kaya, H.; Chan, H. S. Simple Two-State Protein Folding Kinetics Requires Near-Levinthal Thermodynamic Cooperativity. *Proteins* **2003**, *52*, 510−523.
(140) Kaya, H.; Liu, Z.; Chan, H. S. Chevron Behavior and Isostable Enthalpic Barriers in Protein Folding: Successes and Limitations of Simple Gō-Like Modeling. *Biophys. J.* **2005**, *89*, 520−535.
(141) Liu, Z.; Chan, H. S. Solvation and Desolvation Effects in Protein Folding: Native Flexibility, Kinetic Cooperativity, and Enthalpic Barriers under Isostability Conditions. *Phys. Biol.* **2005**, *2*, S75−S85.
(142) Kharakoz, D. P. Volumetric Properties of Proteins and their Analogs in Diluted Water Solutions. 2. Partial Adiabatic Compressibilities of Amino Acids at 15−70°C. *J. Phys. Chem.* **1991**, *95*, 5634−5642.
(143) Dadarlat, V. M.; Post, C. B. Decomposition of Protein Experimental Compressibility into Intrinsic and Hydration Shell Contributions. *Biophys. J.* **2006**, *91*, 4544−4554.
(144) Klapper, M. H. Nature of Protein Interior. *Biochim. Biophys. Acta* **1971**, *229*, 557−566.
(145) Kharakoz, D. P. Protein Compressibility, Dynamics, and Pressure. *Biophys. J.* **2000**, *79*, 511−525.
(146) Dadarlat, V. M.; Post, C. B. Insights into Protein Compressibility from Molecular Dynamics Simulations. *J. Phys. Chem. B* **2001**, *105*, 715−724.
(147) Kell, G. S. Density, Thermal Expansivity, and Compressibility of Liquid Water from 0° to 150°C: Correlations and Tables for Atmospheric Pressure and Saturation Reviewed and Expressed on 1968 Temperature Scale. *J. Chem. Eng. Data* **1975**, *20*, 97−105.
(148) Weir, C. E.; Hoffman, J. D. Compressibilities of Long-Chain Normal Hydrocarbons. *J. Res. Natl. Bur. Stand.* **1955**, *55*, 307−310.
(149) Chalikian, T. V.; Breslauer, K. J. Compressibility as a Means to Detect and Characterize Globular Protein States. *Proc. Natl. Acad. Sci. U.S.A.* **1996**, *93*, 1012−1014.
(150) Jorgensen, W. L.; Buckner, J. K.; Boudon, S.; Tirado-Rives, J. Efficient Computation of Absolute Free Energies of Binding by Computer Simulations: Application to the Methane Dimer in Water. *J. Chem. Phys.* **1988**, *89*, 3742−3746.
(151) Jorgensen, W. L. *BOSS*, version 4.1; Yale University: New Haven, CT, 1999.
(152) Abascal, J. L. F.; Vega, C. A General Purpose Model for the Condensed Phases of Water: TIP4P/2005. *J. Chem. Phys.* **2005**, *123*, 234505.
(153) Pi, H. L.; Aragones, J. L.; Vega, C.; Noya, E. G.; Abascal, J. L. F.; Gonzalez, M. A.; McBride, C. Anomalies in Water as Obtained from Computer Simulations of the TIP4P/2005 Model: Density Maxima, and Density, Isothermal Compressibility and Heat Capacity Minima. *Mol. Phys.* **2009**, *107*, 365−374.
(154) Jorgensen, W. L.; Jenson, C. Temperature Dependence of TIP3P, SPC, and TIP4P water from NPT Monte Carlo Simulations: Seeking Temperatures of Maximum Density. *J. Comput. Chem.* **1998**, *19*, 1179−1186.
(155) Motakabbir, K. A.; Berkowitz, M. Isothermal Compressibility of SPC/E Water. *J. Phys. Chem.* **1990**, *94*, 8359−8362.
(156) Horn, H. W.; Swope, W. C.; Pitera, J. W.; Madura, J. D.; Dick, T. J.; Hura, G. L.; Head-Gordon, T. Development of An Improved Four-Site Water Model for Biomolecular Simulations: TIP4P-Ew. *J. Chem. Phys.* **2004**, *120*, 9665−9678.

(157) Kharakoz, D. P. Volumetric Properties of Proteins and Their Analogs in Diluted Water Solutions. 1. Partial Volumes of Amino Acids at 15−55°C. *Biophys. Chem.* **1989**, *34*, 115−125.
(158) Hnědkovský, L.; Wood, R. H.; Majer, V. Volumes of Aqueous Solutions of CH_4, CO_2, H_2S, and NH_3 at Temperatures from 298.15 to 705 K and Pressures to 35 MPa. *J. Chem. Thermodyn.* **1996**, *26*, 125−142.
(159) Lin, C.-L.; Wood, R. H. Prediction of the Free Energy of Dilute Aqueous Methane, Ethane, and Propane at Temperatures from 600 to 1200°C and Densities from 0 to 1 g cm^{-3} using Molecular Dynamics Simulations. *J. Phys. Chem.* **1996**, *100*, 16399−16409.
(160) Flyvbjerg, H.; Petersen, H. S. Error Estimates on Averages of Correlated Data. *J. Chem. Phys.* **1989**, *91*, 461−466.
(161) Conway, B. E.; Verrall, R. E. Partial Molar Volumes and Adiabatic Compressibilities of Tetraalkylammonium and Aminium Salts in Water. I. Compressibility Behavior. *J. Phys. Chem.* **1966**, *70*, 3952−3961.
(162) Conway, B. E.; Ayranci, E. Structural Effects in the Partial Molar Volumes and Isentropic Compressibilities of Organic Bases and their Conjugate Ions. *J. Chem. Thermodyn.* **1988**, *3*, 9−27.
(163) Sarvazyan, A. P.; Chalikian, T. V. Relationship Between Nonlinear Acoustic Properties and Thermodynamic Characteristics of Solutions of Biological Substances. In *Ultrasonics International 89 Conference Proceedings*; Butterworth Scientific, Madrid, Spain, 1989; pp 704−710.
(164) Millero, F. J.; Lo Surdo, A.; Shin, C. Apparent Molal Volumes and Adiabatic Compressibilities of Aqueous Amino Acids at 25°C. *J. Phys. Chem.* **1978**, *82*, 784−792.
(165) Iqbal, M.; Verrall, R. E. Implications of Protein Folding: Additivity Schemes for Volumes and Compressibilities. *J. Biol. Chem.* **1988**, *263*, 4159−4165.
(166) Hedwig, G. R. Partial Molar Heat Capacities Volumes and Compressibilities of Aqueous Solutions of some Peptides that Model Side-Chains of Proteins. *Pure Appl. Chem.* **1994**, *66*, 387−392.
(167) Mathieson, J. G.; Conway, B. E. Partial Molal Compressibilities of Salts in Aqueous Solution and Assignment of Ionic Contributions. *J. Solution Chem.* **1974**, *3*, 455−477.
(168) Chalikian, T. V.; Sarvazyan, A. P.; Breslauer, K. J. Hydration and Partial Compressibility of Biological Compounds. *Biophys. Chem.* **1994**, *51*, 89−109.
(169) Häckel, M.; Hinz, H.-J.; Hedwig, G. R. Partial Molar Volumes of Proteins: Amino Acid Side-Chain Contributions Derived from the Partial Molar Volumes of Some Tripeptides over the Temperature Range 10−90°C. *Biophys. Chem.* **1999**, *82*, 35−50.
(170) Graziano, G. Hydrostatic Pressure Effect on Hydrophobic Hydration and Pairwise Hydrophobic Interaction of Methane. *J. Chem. Phys.* **2014**, *140*, 094503.
(171) Southall, N. T.; Dill, K. A. *Biophys. Chem.* **2002**, *101*, 295−307.
(172) Richards, F. M. Areas, Volumes, Packing, and Protein Structure. *Annu. Rev. Biophys. Bioeng.* **1977**, *6*, 151−176.
(173) Connolly, M. L. Analytical Molecular Surface Calculation. *J. Appl. Crystallogr.* **1983**, *16*, 548−558.
(174) Lee, B.; Richards, F. M. Interpretation of Protein Structures: Estimation of Static Accessibility. *J. Mol. Biol.* **1971**, *51*, 379−400.
(175) Fennell, C. J.; Kehoe, C. W.; Dill, K. A. Oil/Water Transfer Is Partly Driven by Molecular Shape, Not Just Size. *J. Am. Chem. Soc.* **2010**, *132*, 234−240.
(176) Fennell, C. J.; Kehoe, C. W.; Dill, K. A. Modeling Aqueous Solvation with Semi-Explicit Assembly. *Proc. Natl. Acad. Sci. U.S.A.* **2011**, *108*, 3234−3239.
(177) Blandamer, M. J.; Davis, M. I.; Douhéret, F.; Reis, J. C. R. Apparent Molar Isentropic Compressions and Expansions of Solutions. *Chem. Soc. Rev.* **2001**, *30*, 8−15.
(178) Hillson, M.; Onuchic, J. N.; García, A. E. Pressure-Induced Protein-Folding/Unfolding Kinetics. *Proc. Natl. Acad. Sci. U.S.A.* **1999**, *96*, 14848−14853.
(179) Perezzan, R.; Rey, A. Simulating Protein Unfolding Under Pressure with a Coarse-Grained Model. *J. Chem. Phys.* **2012**, *137*, 185102.
(180) *CRC Handbook of Chemistry and Physics*, 92nd ed.; Haynes, W. M., Ed.; CRC Pressure: Boca Raton, FL, 2011.
(181) Cheng, V. M.; Daniels, W. B.; Crawford, R. K. Melting Parameters of Methane and Nitrogen from 0 to 10 kbar. *Phys. Rev. B* **1975**, *11*, 3972−3975.
(182) Costantino, M. S.; Daniels, W. B. Dielectric Constant of Compressed Solid Methane at Low Temperature. *J. Chem. Phys.* **1975**, *62*, 764−770.
(183) Kammeyer, C. W.; Whitman, D. R. Quantum Mechanical Calculation of Molecular Radii. I. Hydrides of Elements of Periodic Groups IV Through VII. *J. Chem. Phys.* **1972**, *56*, 4419−4421.
(184) Roche, J.; Dellarole, M.; Caro, J. A.; Guca, E.; Norberto, D. R.; Yang, Y.; Garcia, A. E.; Roumestand, C.; García-Moreno, B.; Royer, C. A. Remodeling of the Folding Free Energy Landscape of *Staphylococcal* Nuclease by Cavity-Creating Mutations. *Biochemistry* **2012**, *51*, 9535−9546.
(185) Roche, J.; Dellarole, M.; Caro, J. A.; Norberto, D. R.; García, A. E.; García-Moreno, B.; Roumestand, C.; Royer, C. A. Effect of Internal Cavities on Folding Rates and Routes Revealed by Real-Time Pressure-Jump NMR Spectroscopy. *J. Am. Chem. Soc.* **2013**, *135*, 14610−14618.
(186) Neumaier, S.; Buttner, M.; Bachmann, A.; Kiefhaber, T. Transition State and Ground State Properties of the Helix-Coil Transition in Peptides Deduced from High-Pressure Studies. *Proc. Natl. Acad. Sci. U.S.A.* **2013**, *110*, 20988−20993.
(187) Prigozhin, M. B.; Liu, Y.; Wirth, A. J.; Kapoor, S.; Winter, R.; Schulten, K.; Gruebele, M. Misplaced Helix Slows Down Ultrafast Pressure-Jump Protein Folding. *Proc. Natl. Acad. Sci. U.S.A.* **2013**, *110*, 8087−8092.
(188) Okumura, H. Temperature and Pressure Denaturation of Chignolin: Folding and Unfolding Simulation by Multibaric-Multithermal Molecular Dynamics Method. *Proteins: Struct., Funct., Bioinf.* **2012**, *80*, 2397−2416.
(189) Knott, M.; Chan, H. S. Criteria for Downhill Protein Folding: Calorimetry, Chevron Plot, Kinetic Relaxation, and Single-Molecule Radius of Gyration in Chain Models with Subdued Degrees of Cooperativity. *Proteins: Struct., Funct., Bioinf.* **2006**, *65*, 373−391.
(190) Badasyan, A.; Liu, Z.; Chan, H. S. Probing Possible Downhill Folding: Native Contact Topology Likely Places a Significant Constraint on the Folding Cooperativity of Proteins with ∼ 40 Residues. *J. Mol. Biol.* **2008**, *384*, 512−530.
(191) Taylor, M. P.; Paul, W.; Binder, K. All-Or-None Proteinlike Folding Transition of a Flexible Homopolymer Chain. *Phys. Rev. E* **2009**, *79*, 050801(R).
(192) Kayatekin, C.; Cohen, N. R.; Matthews, C. R. Enthalpic Barriers Dominate the Folding and Unfolding of the Human Cu, Zn Superoxide Dismutase Monomer. *J. Mol. Biol.* **2012**, *424*, 192−202.
(193) Hedoux, A.; Guinet, Y.; Paccou, L. Analysis of the Mechanism of Lysozyme Pressure Denaturation from Raman Spectroscopy Investigations, and Comparison with Thermal Denaturation. *J. Phys. Chem. B* **2011**, *115*, 6740−6748.
(194) Grigera, J. R.; McCarthy, A. N. The Behavior of the Hydrophobic Effect under Pressure and Protein Denaturation. *Biophys. J.* **2010**, *98*, 1626−1631.
(195) Sumi, T.; Sekino, H. Possible Mechanism Underlying High-Pressure Unfolding of Proteins: Formation of a Short-Period High-Density Hydration Shell. *Phys. Chem. Chem. Phys.* **2011**, *13*, 15829−15832.
(196) Das, P.; Matysiak, S. Direct Characterization of Hydrophobic Hydration during Cold and Pressure Denaturation. *J. Phys. Chem. B* **2012**, *116*, 5342−5348.
(197) Sarma, R.; Paul, S. Effect of Pressure on the Solution Structure and Hydrogen Bond Properties of Aqueous *N*-Methylacetamide. *Chem. Phys.* **2012**, *407*, 115−123.
(198) Baldwin, R. L. In Search of the Energetic Role of Peptide Hydrogen Bonds. *J. Biol. Chem.* **2003**, *278*, 17581−17588.
(199) Jorgensen, W. L. Interactions Between Amides in Solution and the Thermodynamics of Weak Binding. *J. Am. Chem. Soc.* **1989**, *111*, 3770−3771.

(200) Petrauskas, V.; Gylyte, J.; Toleikis, Z.; Cimmperman, P.; Matulis, D. Volume of Hsp90 Ligand Binding and the Unfolding Phase Diagram as a Function of Pressure and Temperature. *Eur. Biophys. J.* **2013**, *42*, 355−362.
(201) Cheung, J. K.; Shah, P.; Truskett, T. M. Heteropolymer Collapse Theory for Protein Folding in the Pressure−Temperature Plane. *Biophys. J.* **2006**, *91*, 2427−2435.
(202) Rouget, J.-B.; Schroer, M. A.; Jeworrek, C.; Púhse, M.; Saldana, J.-L.; Bessin, Y.; Tolan, M.; Barrick, D.; Winter, R.; Royer, C. A. Unique Features of the Folding Landscape of a Repeat Protein Revealed by Pressure Perturbation. *Biophys. J.* **2010**, *98*, 2712−2721.
(203) Reinhardt, M.; Dzubiella, J.; Trapp, M.; Gutfreund, P.; Kreuzer, M.; Gröschel, A. H.; Müller, A. H. E.; Ballauff, M.; Steitz, R. Fine-Tuning the Structure of Stimuli-Responsive Polymer Films by Hydrostatic Pressure and Temperature. *Macromolecules* **2013**, *46*, 6541−6547.